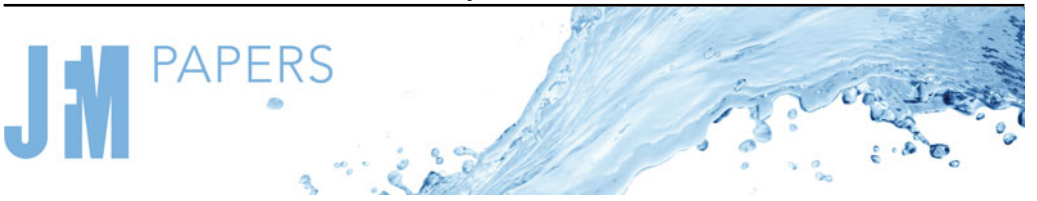
J. Fluid Mech. (2026), *vol.* 1028, A49, doi:10.1017/jfm.2026.11161



Self-regulating non-equilibrium in a slender body's turbulent wake

Gagan Kewalramani[1,2], **Clément Barbet-Lavergne**[1], **Pierre Bragança**[1], **Christophe Cuvier**[1] **and John Christos Vassilicos**[1]

[1]Univ. Lille, CNRS, ONERA, Arts et Metiers Institute of Technology, Centrale Lille, UMR 9014, LMFL – Laboratoire de Mécanique des Fluides de Lille, Kampé de Fériet, F-59000 Lille, France

[2]Department of Mechanical Engineering, Indian Institute of Technology-Jodhpur, Rajasthan, India

Corresponding authors: Gagan Kewalramani, gagan.kewalramani@gmail.com; John Christos Vassilicos, john-christos.vassilicos@cnrs.fr

(Received 10 March 2025; revised 10 November 2025; accepted 1 January 2026)

We study transverse profiles and time fluctuations of turbulence dissipation rate, turbulence kinetic energy and integral length scales by means of high-speed stereoscopic particle image velocimetry in the turbulent wake of a 6 : 1 prolate spheroid that has its principal axis aligned with the incoming non-turbulent flow. This turbulent wake of a slender body differs from turbulent bluff body wakes in terms of transverse non-homogeneity of turbulence dissipation rate and because it is not axisymmetric even though it nominally is. Even so, both transverse profiles and time fluctuations of turbulence dissipation rate coefficients (inverse ratio between the rate with which the large scales lose energy and the rate with which the small scales dissipate energy) and of the Taylor length-based Reynolds number (ratio between the turbulent kinetic energy mostly in the large scales and the turbulent kinetic energy at the smallest scales) obey self-regulating non-equilibrium, as previously found in various other turbulent flows. However, the power law relating the transverse variations and the time fluctuations of these two ratios differs from previously reported self-regulating non-equilibrium power law scalings in other turbulent flows.

Key words: wakes, turbulence theory

1. Introduction

An essential property of turbulence is that it is dissipative. Turbulence dissipation plays a key role in all turbulent flows. The scaling of the turbulence dissipation rate is pivotal in theories and models of turbulent flow statistics and dynamics (e.g. Tennekes & Lumley 1972).

© The Author(s), 2026. Published by Cambridge University Press. This is an Open Access article, distributed under the terms of the Creative Commons Attribution licence (https://creativecommons.org/licenses/by/4.0/), which permits unrestricted re-use, distribution and reproduction, provided the original article is properly cited.

https://doi.org/10.1017/jfm.2026.11161 Published online by Cambridge University Press

The Kolmogorov scale-by-scale equilibrium for homogeneous stationary turbulence leads to a well-known expression for the turbulence dissipation rate ϵ (Batchelor 1953; Tennekes & Lumley 1972; Sreenivasan 1984; Frisch 1995): $\epsilon = C_\epsilon k^{3/2}/L$, where k is the turbulent kinetic energy, L is a measure of the largest turbulent eddies in the flow (an integral length scale) and C_ϵ is a dimensionless coefficient independent of Reynolds number. The Kolmogorov equilibrium means that the average rate $C_\epsilon k^{3/2}/L$ with which the large turbulent eddies lose energy to smaller eddies equals the average rate with which the turbulence loses energy by viscous dissipation. However, a different turbulence dissipation scaling has emerged over the past 15 years in various turbulent flows where non-stationarity (including streamwise decay/non-homogeneity) cannot be overlooked: freely decaying periodic turbulence (Goto & Vassilicos 2016*b*) where a significantly long early time range exists where C_ϵ grows while the Taylor length-based Reynolds number decreases; and decaying turbulence generated by fractal or regular grids (Vassilicos 2015), turbulent bluff body wakes (Castro 2016) and turbulent jets (Cafiero & Vassilicos 2019) where a long centreline near-region exists where C_ϵ increases whilst Re_λ decreases along the streamwise direction. In all these cases, C_ϵ and Re_λ vary according to $C_\varepsilon \sim \sqrt{Re_G}/Re_\lambda$, where Re_G is some global Reynolds number characterising inlet/initial/boundary conditions. Time fluctuations of C_ϵ and Re_λ in forced periodic turbulence (Goto & Vassilicos 2015; Goto & Vassilicos 2016*a*) and in atmospheric turbulence (Waclawczyk *et al.* 2022*a*, 2022*b*) follow the exact same scaling: C_ϵ increases as Re_λ decreases and C_ϵ decreases as Re_λ increases following $C_\varepsilon \sim \sqrt{Re_G}/Re_\lambda$.

Whilst the non-equilibrium dissipation scaling $C_\varepsilon \sim \sqrt{Re_G}/Re_\lambda$ seems to define a rather wide universality class of time fluctuations and streamwise profiles, it is not fully universal. A similar anticorrelation in time fluctuations of the Taylor length-based Reynolds number and various definitions of C_ϵ was found in fully developed turbulent channel flow (Apostolidis, Laval & Vassilicos 2022) but following a power law with slightly different exponents between -1 and $-3/2$ (depending on C_ϵ definition and wall distance) as opposed to the -1 exponent in $C_\varepsilon \sim \sqrt{Re_G}\,Re_\lambda^{-1}$. It has also been claimed that the streamwise profiles of C_ϵ and Re_λ (obtained from time and azimuthally averaged quantities) in a non-equilibrium region downstream of a slender rather than bluff body are related by $C_\varepsilon \sim (\sqrt{Re_G}/Re_\lambda)^n$ with $n = 4/3$ rather than $n = 1$ at high enough global Reynolds numbers (Ortiz-Tarin, Nidhan & Sarkar 2021).

Opposite trends between local Reynolds number and local turbulence dissipation coefficient (i.e. one grows while the other one decays) is not found only in time fluctuations and streamwise profiles but also in transverse spatial profiles. This was shown by Chen *et al.* (2021) and Alves-Portela & Vassilicos (2022) who studied transverse profiles of time-average turbulent kinetic energy, turbulence dissipation rate and integral scale at various streamwise locations in three qualitatively different turbulent wakes of pairs of square prisms, in which case the reported power law exponent n is between 1.3 and 1.5. There seems to be a qualitative universality in non-stationarity and non-homogeneity: C_ε^{-1} is the ratio between the rate $k^{3/2}/L$ with which the large scales lose energy and the rate ϵ with which the small scales dissipate energy, whereas Re_λ is the ratio between the turbulent kinetic energy k mostly in the large scales and the turbulent kinetic energy $\sqrt{\nu\varepsilon}$ at the smallest scales (ν is the fluid's kinematic viscosity). The universal property seems to be that, when C_ϵ is not constant, these two ratios increase and decrease together, whether in time or space, in a wide range of turbulent flows. As already noted by Vassilicos & Laval (2024), the strong anticorrelation or opposite trends between C_ϵ and Re_λ suggests that the turbulence non-equilibrium between $k^{3/2}/L$ and ϵ is self-regulating (the term 'self-regulating' in the context of the turbulence cascade was first used by Steiros 2021).

https://doi.org/10.1017/jfm.2026.11161 Published online by Cambridge University Press

When turbulent kinetic energy decays slower at the large scales than at the small scales, the rate of loss of energy grows faster at the large scales than at the small scales; and when turbulent kinetic energy decays faster at the large scales than at the small scales, the rate of loss of turbulent kinetic energy grows more slowly at the large scales than at the small scales. Kolmogorov equilibrium is not designed for non-stationary and/or non-homogeneous turbulence, yet some qualitative universality may exist for such non-equilibrium turbulence. Note that, even though the values of the exponent n reported till now in the literature are between approximately 1 and 1.5, *a priori* any $n > 0$ satisfies the necessary condition for self-regulating non-equilibrium.

A couple of years ago, Zheng *et al.* (2023*a*) and (2023*b*) studied experimentally the time fluctuations of turbulence dissipation rate, integral scale and turbulent kinetic energy in the turbulence downstream of both regular and active grids. They demonstrated that these fluctuations are in self-regulating non-equilibrium both where the streamwise evolution of their time averages is self-regulating and where it is not. Earlier experiments by Mora *et al.* (2019) and Zheng, Nagata & Watanabe (2021) had shown that C_ϵ (obtained from long time averages) remains constant while Re_λ (also obtained from long time averages) decays along streamwise space in active grid-generated turbulence. Such absence of streamwise self-regulation also exists in regular grid-generated turbulence but only in the far field (Vassilicos 2015): upstream of this far field, C_ϵ (obtained from long time averages) increases whilst Re_λ (also obtained from long time averages) decreases following $C_\varepsilon \sim \sqrt{Re_G}/Re_\lambda$ in the streamwise direction. It does not matter whether the time fluctuations are probed in a region of grid-generated turbulence where streamwise variations follow $C_\epsilon \sim \sqrt{Re_G}/Re_\lambda$ or in a region where C_ϵ remains constant as Re_λ varies in the streamwise direction (streamwise variations for time average quantities), these time fluctuations are in self-regulating non-equilibrium and follow the same scaling $C_\epsilon \sim \sqrt{Re_G}/Re_\lambda$ but in time, both in regular and active grid-generated turbulence (Zheng *et al.* 2023*a*, 2023*b*).

To our best knowledge, self-regulating non-equilibrium has never been studied experimentally in the turbulent wake of a slender rather than bluff body. In this paper we report analyses of high-speed stereo particle image velocimetry (SPIV) data taken in the turbulent wake of a 6 : 1 prolate spheroid with its principal axis aligned with the streamwise direction, the exact case of a slender body wake simulated with high-fidelity large eddy simulations by Ortiz-Tarin *et al.* (2021). These authors found evidence of self-regulating non-equilibrium in streamwise profiles but did not study transverse profiles and time fluctuations at various positions in the flow. Our high-speed SPIV measurements are taken in transverse planes at four streamwise positions and we concentrate attention on self-regulating non-equilibrium in transverse profiles and time fluctuations at various spatial positions in the flow. Our study of time fluctuations follows the methodology introduced by Zheng *et al.* (2023*a*) and (2023*b*). As explained in § 4.4, this methodology presents the important advantage of plotting quantities in a way that significantly increases signal to noise ratio. Additionally, the high-speed nature of our spatially resolved SPIV can be exploited for noise reduction of turbulence dissipation rate estimates. This denoising procedure is detailed in § 2.

The paper is organised as follows. The experimental procedure is presented in § 2 and a detailed characterisation of the flow is given in § 3. Spatial profiles and time fluctuations of turbulence dissipation rate, turbulent kinetic energy and integral scales are studied in § 4, where a detailed assessment of self-regulating non-equilibrium is made. Our main conclusions are summarised in § 5.

https://doi.org/10.1017/jfm.2026.11161 Published online by Cambridge University Press

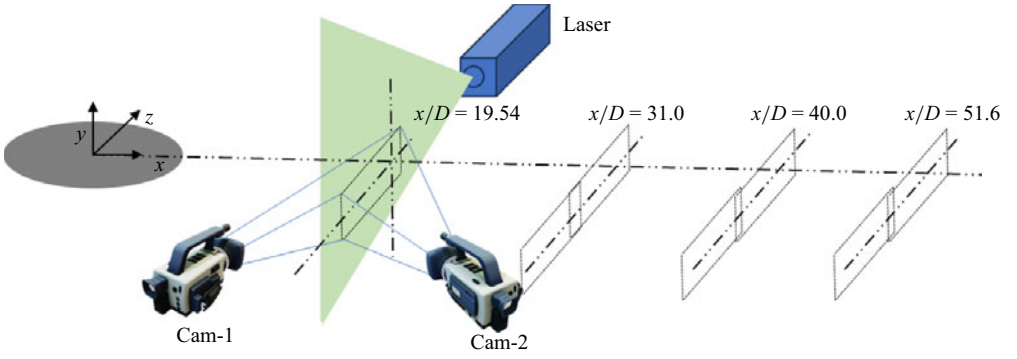


Figure 1. Schematic of the experimental measurement set-up for stereo-PIV measurement.

x/D	ϵ_{hw} ($m^2\ s^{-3}$)	η_k (mm)	SPIV IW size ($\delta z \times \delta y$)	Thickness of laser (δx)	$\overline{U}\Delta t$	ϵ surrogates (% difference with ϵ_{hw})		
						ϵ_{iso1}	ϵ_{iso2}	ϵ in (2.1)
19.54	0.353	0.30	$3.1\eta_k \times 3.1\eta_k$	$6.6\eta_k$	$2.1\eta_k$	0.304 (−14.9)	0.51 (36.3)	0.304 (−16.9)
31.00	0.117	0.40	$2.3\eta_k \times 2.3\eta_k$	$5\eta_k$	$1.7\eta_k$	0.133 (12.8)	0.121 (−9.1)	0.106 (−7.8)
40.00	0.041	0.48	$1.9\eta_k \times 1.9\eta_k$	$4.16\eta_k$	$1.36\eta_k$	0.038 (−9.6)	0.043 (4.76)	0.038 (−11.7)
51.60	0.029	0.57	$1.6\eta_k \times 1.6\eta_k$	$3.5\eta_k$	$1.15\eta_k$	0.0243 (−18.16)	0.032 (9.84)	0.023 (4.16)

Table 1. Turbulence kinetic energy dissipation rate measurement parameters and estimations on the centreline. Here, ϵ_{hw} is the turbulent dissipation rate calculated on the geometric centreline of the wake from HWA and η_k is $(\nu^3/\epsilon_{hw})^4$. The averaging size of the IW, δx, δy and δz, is stated in terms of η_k.

2. Experimental methodology

Experiments on the wake of a 6 : 1 prolate spheroid were conducted in the LMFL wind tunnel (see Carlier & Stanislas 2005 for details). The 6 : 1 prolate spheroid's diameter at its centre ($x, y, z = 0$) is 80 mm and its length along the principal axis is 480 mm. Experiments were conducted with inlet velocity $U_0 = 9$ m sec^{-1} and an inlet Reynolds number $Re(\equiv U_0 D/\nu)$ equal to 4.8×10^4. The inlet velocity and the spheroid's principal axis are aligned with the streamwise (x) direction. The x, y and z directions are shown in the schematic of the experimental set-up in figure 1.

Single-point hot-wire anemometry (HWA) and high-speed SPIV measurements were performed at four streamwise locations that are $x/D =$ 19.54, 31, 40 and 51.6. The HWA measurements were performed on the geometric centreline ($y, z = 0$) only and the resulting centreline isotropic surrogate of the turbulent dissipation rate $\epsilon_{hw} \equiv 15\nu/\bar{U}^2\overline{(\partial u'/\partial t)^2}$ (assuming small-scale isotropy and Taylor's frozen turbulence hypothesis, $\bar{U}$ being the streamwise mean velocity at the spatial location where the measurement is made) and Kolmogorov length $\eta_k = (\nu^3/\epsilon_{hw})^{1/4}$ are given in table 1 (ν is the fluid's kinematic viscosity). Stereo-PIV provided measurements of the three components of velocity, u (x direction), v (y direction) and w (z direction), by using two cameras focused on the common measurement region and a high-speed laser. The schematic of the experimental set-up with the laser and the two cameras recording images in the transverse $y-z$ plane (normal to the streamwise direction) is shown in figure 1. Note that the recording in forward scattering mode ensures maximum illumination of seeding particles at the camera sensor.

The SPIV measurements were high speed and performed at 14 kHz by using two lasers at 7 kHz each (the time Δt between consecutive images is such that $1/\Delta t = 14$ kHz).

https://doi.org/10.1017/jfm.2026.11161 Published online by Cambridge University Press

An Nd:YLF laser from Quantronix with M^2 (beam quality) around 20 and two CMOS cameras (Phantom 340) of 10 μm pixels sensor size were used in the SPIV measurement. The laser sheet was 2 mm thick and ensured sufficient overlap of seeding particles for the SPIV cross-correlation. The wake deficit region grows with streamwise distance. As a result, larger fields of view are needed further downstream. At $x/D = 19.54$ the field of view is 72 mm long (in the z direction) and 8.8 mm wide (in the y direction), but an additional SPIV measurement plane with an offset of $z = +60$ mm was also recorded at $x/D = 31.00$, 40.00 and 51.60 as shown in figure 1. Hence, at $x/D = 19.54$ the field of view is made of one measurement plane and covers the coordinates $y = [-4 \text{ to } 4]$ mm and $z = [-6.2 \text{ to } 65.8]$ mm whereas at $x/D = 31.00$, 40.00 and 51.60 the field of view is made of two measurement planes and covers the coordinates $y = [-4 \text{ to } 4]$ mm and $z = [-6.2$ to 125.8] mm.

Taylor's frozen turbulence hypothesis has been used in this paper both on HWA and SPIV data. It states that if the turbulent eddies have not significantly evolved as they advect, the streamwise velocity derivative can be approximated from the temporal derivative, i.e. $(\partial/\partial x) = (1/\bar{U}) \cdot (\partial/\partial t)$. For Taylor's frozen turbulence hypothesis to be valid, the turbulence intensity should be below 10 %–15 % and the mean streamwise velocity component (x direction here) should be much larger than the mean transverse velocity components (y and z directions here); see, for example, Gledzer (1997) and references therein. Throughout our PIV measurement regions (which include the geometric centreline where HWA measurements were made), the mean streamwise velocity was an order of magnitude larger than the mean transverse velocities, and turbulent velocity was also below or at most 2.5 % of the mean velocity (see also figure 3(*b*) noting that the centreline streamwise mean velocity deficit U_d is an order of magnitude smaller than $\bar{U}$). Out-of-plane derivatives $(\partial/\partial x)$ were therefore calculated from temporal derivatives $(\partial/\partial t)$ by using Taylor's frozen turbulence hypothesis. (Since we are using two distinct lasers (each at 7 KHz to get 14 KHz acquisition), temporal derivatives are calculated using a central differencing scheme over the time interval $2\Delta t$. This ensures that the same laser is used in temporal derivative calculations, which avoids errors on derivative calculations caused by minor differences in the two distinct laser characteristics.)

The study of self-regulating non-equilibrium requires measurements of turbulent kinetic energies, integral scales and turbulent dissipation rates. Stereo-PIV allows access to the full turbulent kinetic energy in the entire field of view. Fields of integral scales are obtained as described at the start of § 4 by integrating autocorrelation functions over time. Accurate estimation of derivatives of fluctuating velocities at high spatial resolution is required for extracting turbulence dissipation rates from our data given

$$\epsilon = \nu \left(2 \left[\overline{\left(\frac{\partial u'}{\partial x}\right)^2} + \overline{\left(\frac{\partial v'}{\partial y}\right)^2} + \overline{\left(\frac{\partial w'}{\partial z}\right)^2} \right] + 2 \left[\overline{\frac{\partial u'}{\partial y}\frac{\partial v'}{\partial x}} + \overline{\frac{\partial u'}{\partial z}\frac{\partial w'}{\partial x}} + \overline{\frac{\partial w'}{\partial y}\frac{\partial v'}{\partial z}} \right] + \left[\overline{\left(\frac{\partial u'}{\partial y}\right)^2} + \overline{\left(\frac{\partial v'}{\partial x}\right)^2} + \overline{\left(\frac{\partial u'}{\partial z}\right)^2} + \overline{\left(\frac{\partial w'}{\partial x}\right)^2} + \overline{\left(\frac{\partial v'}{\partial z}\right)^2} + \overline{\left(\frac{\partial w'}{\partial y}\right)^2} \right] \right), \quad (2.1)$$

where the overbars signify time averaging and u', v' and w' are the fluctuating velocities obtained from u, v and w, respectively, after Reynolds decomposition. For statistical convergence of our statistics, at all four x/D positions of our measurements, we recorded 66 experimental runs each having a recording time of 3 sec and have checked that all the statistics presented in this paper are fully converged.

Images with a mean spatial resolution of 52 μm pixel size are processed with an in-house four-pass adaptive window PIV processing method (detailed in Beaumard

https://doi.org/10.1017/jfm.2026.11161 Published online by Cambridge University Press

et al. (2024)). This PIV processing results in a velocity field that is averaged over an interrogation window (IW) of size 16 × 24 pixels and an overlap of around 58 %. A Cubic b-spline interpolation using grey level and bilinear interpolation image deformation (Scarano 2001; Lecordier & Trinite 2004) was also used before the final pass. The model described in Soloff, Adrian & Liu (1997) was used to calculate the magnitude of all three components of velocity from two planar PIV results from two cameras. To account for corrections due to misalignment between the light sheet and the calibration plane, the self-calibration correction method (Coudert & Schon 2001; Wieneke 2005) is also used in the SPIV processing. The IW size in terms of η_k is stated in table 1. For estimation of ϵ, a spatial resolution (i.e. IW size) of around $4\eta_k$ or below is usually considered sufficient (see Lavoie *et al.* 2007; Tokgoz *et al.* 2012; Laizet, Nedić & Vassilicos 2015). Our transverse plane spatial resolutions δz and δy are all below $4\eta_k$, as can seen in table 1.

The thickness of the laser sheet is such that the IW size δx in the streamwise direction varies from $6.6\eta_k$ to $3.5\eta_k$ with increasing x/D measurement position (see table 1). However, Zaripov, Li & Dushin (2019) have demonstrated in a turbulent boundary layer that the turbulence dissipation rate can be estimated sufficiently accurately with a IW size larger in the direction of smallest variation (streamwise here) than in the other directions.

The small-scale resolution of our SPIV is necessary but not sufficient to ensure accurate ϵ estimation because of the noise contamination of the measured velocities. One of the major sources of noise results from the approximation of the location of the seeding particles in the pixelised images (as explained in the supplementary material of Beaumard *et al.* 2024). To eliminate this noise in the estimation of ϵ, Beaumard *et al.* (2024) proposed the use of high-speed PIV (or SPIV in our case) and calculation of squares of fluctuating velocity derivatives as products of fluctuating velocity derivatives at the same location but nearby times. Beaumard *et al.* (2024) argued that the noise in these derivatives taken at the same location decorrelates very quickly with time whereas the signal does not. Hence, if the time separation is small enough for the signal to remain effectively the same but large enough for the noise to decorrelate sharply, the products of fluctuating velocity derivatives at nearby times will be suitably denoised estimates of squares of fluctuating velocity derivatives (see also George & Stanislas 2021).

To find the small time separation $n_{sep}\Delta t$ that is appropriate for denoising squares of velocity derivatives obtained from SPIV, we compare the isotropic surrogate ϵ_{hw} of the turbulence dissipation rate obtained from the HWA with two isotropic surrogates of the turbulence dissipation rate ϵ_{iso1} and ϵ_{iso2} obtained from SPIV on the basis of (2.2):

$$\epsilon_{iso1} = \frac{15\nu}{\bar{U}^2}\left[\overline{\left(\frac{\partial u'}{\partial t}\right)_t \cdot \left(\frac{\partial u'}{\partial t}\right)_{(t+n_{sep}\Delta t)}}\right];$$

$$\epsilon_{iso2} = 15\nu\left[\overline{\left(-\frac{\partial v'}{\partial y} - \frac{\partial w'}{\partial z}\right)_t \cdot \left(-\frac{\partial v'}{\partial y} - \frac{\partial w'}{\partial z}\right)_{t+n_{sep}\Delta t}}\right]. \tag{2.2a–b}$$

The isotropic surrogate ϵ_{iso1} is obtained by time averaging the product of $(\partial u'/\partial t)_t$ at time t with $(\partial u'/\partial t)_{t+n_{sep}\Delta t}$ at time $t + n_{sep}\Delta t$; and the isotropic surrogate ϵ_{iso2} is calculated by time averaging the product of $(-(\partial v'/\partial y) - (\partial w'/\partial z))_t$ at time t with $(-(\partial v'/\partial y) - (\partial w'/\partial z))_{t+n_{sep}\Delta t}$ at time $t + n_{sep}\Delta t$. The quantity ϵ_{iso1} is an estimate of ϵ based on the hypothesis of small-scale isotropy and Taylor's frozen turbulence hypothesis. The quantity ϵ_{iso2} is an estimate of ϵ based on the hypothesis of small-scale isotropy and continuity. Whilst there is of course some uncertainty in the HWA estimate of the isotropic surrogate

https://doi.org/10.1017/jfm.2026.11161 Published online by Cambridge University Press

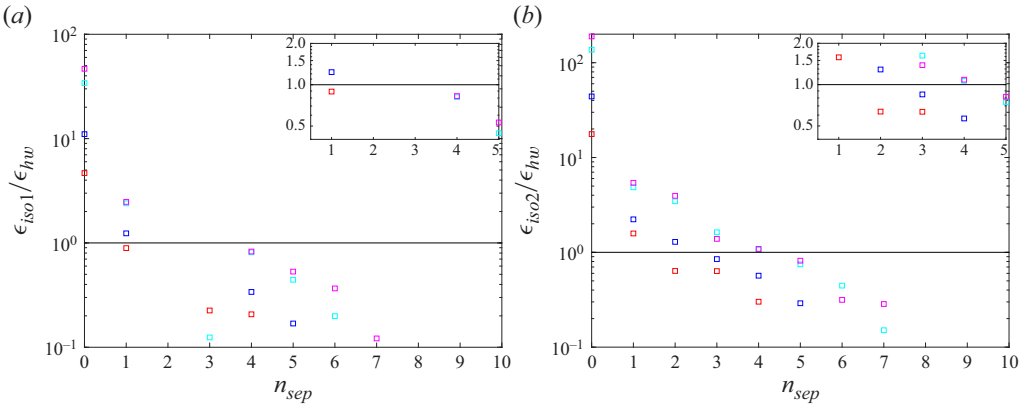


Figure 2. (*a,b*) Comparisons of isotropic surrogates of turbulence dissipation rate from SPIV with ϵ_{hw} from HWA for various temporal separations $n\Delta t$. The results at $x/D = 19.54$, 31.00, 40.0 and 51.6 are shown with □, □, □ and □ symbols, respectively.

of ϵ, it is not as high as the uncertainty caused by the noise in the location of seeding particles in PIV's or SPIV's pixelated images. Indeed, setting $n_{sep} = 0$ leads to order of magnitude differences between ϵ_{hw} and either ϵ_{iso1} or ϵ_{iso2} as can be seen in figure 2. This difference drops dramatically for $n_{sep} = 1$ as can also be seen in figure 2 where we plot the ratios $\epsilon_{iso1}/\epsilon_{hw}$ (panel *a*) and $\epsilon_{iso2}/\epsilon_{hw}$ (panel *b*) versus n_{sep}. As n_{sep} increases, these ratios decrease towards 0 because they increasingly sample the decorrelation in the actual velocity derivative signal itself rather than just in the noise. Note that there are no data for $n_{sep} = 2$ in figure 2(*a*). This is because streamwise derivatives are calculated using a central difference scheme and there can be common velocity components in derivative calculations leading to spurious correlations between velocity gradients at times $n_{sep}\Delta t = 2\Delta t$ apart.

Looking at the two plots (and their inserts) in figure 2 we first see that with $n_{sep} = 1$ (for which $\bar{U} n_{sep}\Delta t/\eta_k$ is between 2.1 and 1.15 depending on x/D; see table 1), the noise in the SPIV estimates is significantly reduced and their order of magnitude is correct at all streamwise locations. For the first two streamwise locations, $x/D = 19.54$ and 31.00, $n_{sep} = 1$ is enough for ϵ_{iso1} to be near-equal to ϵ_{hw}, whereas $n_{sep} = 4$ is significantly better for the further two locations, i.e. $x/D = 40.00$ and 51.60. Similar behaviour is observed for ϵ_{iso2} except that the best value of n_{sep} is now 3 rather than 1 at $x/D = 31.00$. A reason for time separations larger than Δt, i.e. n_{sep} strictly larger than 1, required in some locations may be the larger noise-to-signal ratio as discussed in Appendix A. From the IW sizes (δx) and streamwise separations ($\bar{U}\Delta t$) in table 1, it is evident that after $n_{sep} = 3$ there is no overlap between IWs and, therefore, complete denoising is possible if the turbulent velocity derivatives remain highly correlated as appears to be the case in streamwise locations $x/D = 40.00$ and $x/D = 51.6$; see figure 2. In all our locations, whether n_{sep} equals 1, 3 or 4, it is such that $\bar{U} n\Delta t/\eta_k$ is between 2 and 5. The ratios $\epsilon_{iso1}/\epsilon_{hw}$ and $\epsilon_{iso2}/\epsilon_{hw}$ drop below 1 at normalised time separations $\bar{U} n\Delta t/\eta_k$ larger than 5 or 6, suggesting that the signal starts to decorrelate at such time separations. However, as we have just seen, the noise decorrelates dramatically at time separations smaller than that, i.e. $n_{sep} = 1$, 3 or 4.

From the results for $\epsilon_{iso1}/\epsilon_{hw}$ in figure 2, it can be inferred that the streamwise derivatives $((\partial u_i')/(\partial x))^2$ (for all velocities that are obtained here from our SPIV using Taylor's hypothesis) can be denoised with time separations $n_{sep} =$ 1, 1, 4 and 4 for

https://doi.org/10.1017/jfm.2026.11161 Published online by Cambridge University Press

locations $x/D = 19.54$, 31.00, 41.00 and 51.6, respectively. Similarly from the results for $\epsilon_{iso2}/\epsilon_{hw}$, it can be inferred that the transverse derivatives $((\partial u_i')/(\partial y))^2$ and $((\partial u_i')/(\partial z))^2$ obtained from our SPIV can be denoised with time separations $n_{sep} = 1$, 3, 4 and 4 for locations $x/D = 19.54$, 31.00, 41.00 and 51.6, respectively. In calculating ϵ, all the terms in (2.1) were denoised with separations n_{sep} as explained above. We show in the following section that transverse profiles of ϵ obtained this way conform with expectations. An additional way to increase signal-to-noise ratio, specific to time fluctuations of turbulence dissipation, is presented and used successfully in the third paragraph of § 4.4.

3. Characterisation of the flow

3.1. *Velocity statistics*

The transverse (along z) variation of the time-averaged streamwise velocity $\bar{U}$ at $y = 0$ is shown in figure 3(*a*). The 5 % discontinuity in $\bar{U}$ observed in this plot for $x/D = 31.00$, 40.00 and 51.60 occurs in the merging region of the two measurement planes. At the last three streamwise locations, two distinct SPIV measurements were performed at different times (see figure 1), therefore, manual misalignment of distinct SPIV measurements, optical error due to distortion at the edges of the recording cameras and/or calibration differences can cause this discontinuity that is customary in such dual SPIV set-ups. The mean flow velocity $\bar{U}$ increases in the streamwise and transverse directions. Even in the region $z/D > 1.2$, where the $\bar{U}$ profile is approximately uniform in z, $\bar{U}$ increases slightly with streamwise direction. This increase in $\bar{U}$ is due to the increase in the effective blockage caused by the growth of the boundary layers at the walls of the wind tunnel. However, the streamwise increase of $\bar{U}$ on the wake's geometric centreline is even greater (see figure 3) so that the mean deficit velocity decreases with streamwise distance. The wake half-width $b(x)$ is defined as the transverse distance $z = b(x)$ where the mean velocity deficit has dropped to half its value at the geometrical centre $z = 0$, and it is used to normalise the transverse distance z in our plots.

Transverse profiles (along z/b) of normalised turbulent stresses $(\overline{u_i'u_j'}/U_d^2)$, $(u_i' \equiv u_i - \bar{u}_i$, where the overbar signifies time averaging and U_d is the centreline streamwise mean velocity deficit) are also shown in figure 3(*b,c*). Similar to the mean flow profile, errors (less than 16 %) in the merging region of the two planes are also present in the turbulent stress profile. Just like other canonical free turbulent shear flows, for example, jets (Cafiero & Vassilicos 2019) and wakes (Alves Portela, Papadakis & Vassilicos 2018; Chen *et al.* 2021), the normal turbulent stresses are anisotropic, i.e. $\overline{u'u'}$ is typically larger than both $\overline{v'v'}$ and $\overline{w'w'}$. However, unlike bluff body wakes that are axisymmetric, the wake of our prolate spheroid is not axisymmetric around the prolate spheroid's streamwise axis of symmetry even though it is aligned with the incoming flow. Indeed, figure 3(*b,c*) shows $\overline{v'v'} \neq \overline{w'w'}$ and $\overline{u'v'} \neq \overline{u'w'}$. Whilst $\overline{u'v'}$ and $\overline{v'w'}$ appear negligible, $\overline{u'w'}$ is very significant and its transverse profile shows an off-centre peak as classically observed in turbulent wakes of bluff bodies. This asymmetry has already been observed experimentally by Ashok, Van Buren & Smits (2015) who have attributed it to a kind of swirl in the evolution of the wake generated by a pair of unequal vortices in the wake. The asymmetry is also clearly visible in the turbulent fluxes $\overline{u_i'u_i'u_j'}$ given that $\overline{w'u_i'u_i'}$ and $\overline{v'u_i'u_i'}$ $(w' \equiv u_3', \ v' \equiv u_2')$ are very different for all $i = 1, 2, 3$ (see figure 3*d–f*). The maximum magnitude fluxes of turbulent energy appear around $z/b \approx 1$.

https://doi.org/10.1017/jfm.2026.11161 Published online by Cambridge University Press

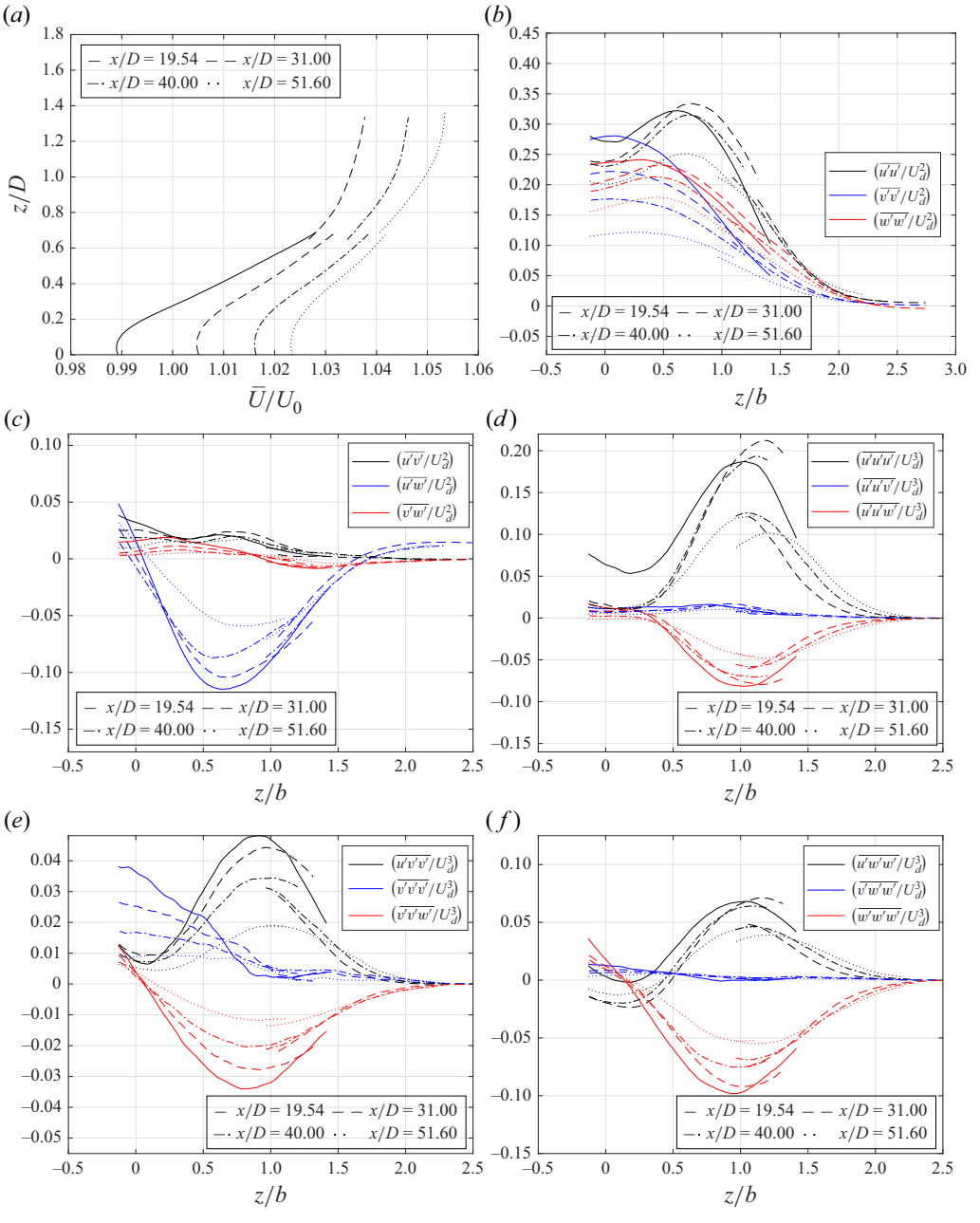


Figure 3. Transverse (z direction) profiles of various one-point velocity statistics. (*a*) The mean velocity in the streamwise direction. (*b*,*c*) Averages of products of two fluctuating velocities. (*d–f*) Averages of products of three fluctuating velocities. The wake half-width is $b = 41$ mm at $x/D = 19.54$, $b = 44$ mm at $x/D = 31.00$, $b = 48$ mm at $x/D = 40.00$ and $b = 51$ mm at $x/D = 51.60$. (Here $D = 80$ mm.)

https://doi.org/10.1017/jfm.2026.11161 Published online by Cambridge University Press

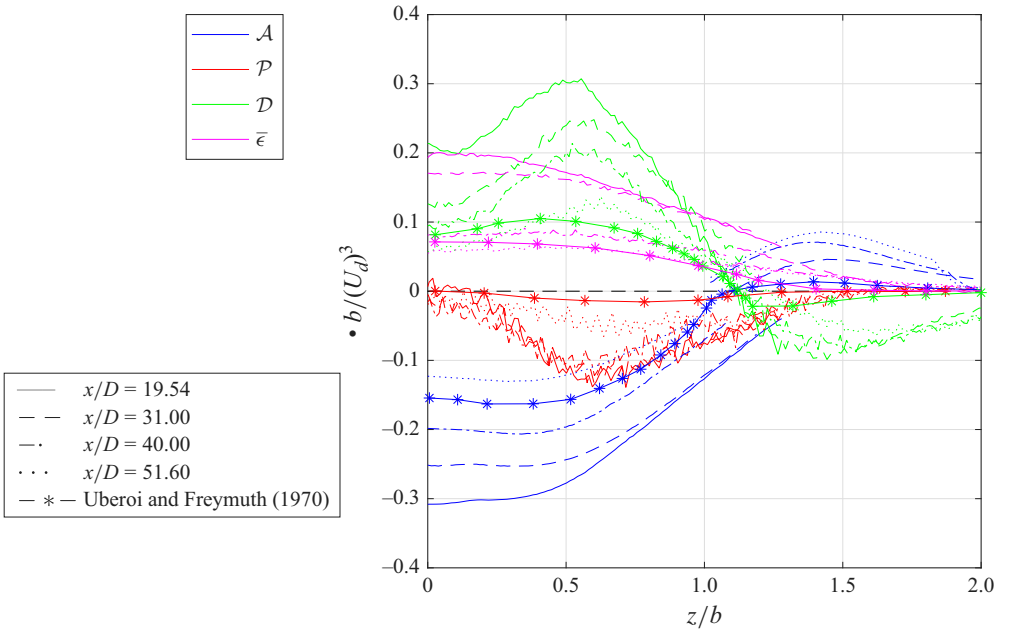


Figure 4. Transverse profiles of $\mathcal{A}$, $\mathcal{P}$ and $\mathcal{D}$ (defined in (3.1)) at four streamwise locations.

3.2. *Averaged one-point turbulent energy advection, transport and production*

Turbulent energy fluxes are part and parcel of the turbulent kinetic energy budget

$$\underbrace{\bar{u}_j \frac{\partial k}{\partial x_j}}_{\mathcal{A}} + \underbrace{\left(\overline{u_i' u_j'}\right) \frac{\partial \bar{u}_i}{\partial x_j}}_{\mathcal{P}} = -\frac{\partial}{\partial x_j}\left(\overline{u_j' p'}\right) - \underbrace{\frac{\partial}{\partial x_j}\left(\frac{\overline{u_j' u_i' u_i'}}{2}\right)}_{\mathcal{D}} + \nu \nabla^2 k - \epsilon, \tag{3.1}$$

where $k \equiv 0.5\overline{u_i' u_i'}$ is the turbulent kinetic energy per unit mass and the overbars signify time averaging (note that the average turbulence dissipation rate ϵ is also obtained by time averaging). The point now is not to further demonstrate the absence of axisymmetry, this asymmetry has already been demonstrated, but to give some idea of how the energetics of our turbulent wake vary with streamwise (x) and transverse (z) distances.

Using the velocity statistics described in § 3.1, the advection ($\mathcal{A}$), production ($\mathcal{P}$) and turbulent transport/diffusion ($\mathcal{D}$) of turbulent kinetic energy (defined in (3.1)) are calculated and plotted in figure 4. The streamwise derivatives ($\partial/\partial x$) are estimated as follows: firstly, the velocity vectors in all four streamwise locations with the same y and z coordinates are fitted by a power law dependence on x and the streamwise derivative at each location is calculated by differentiating the power law fit. Secondly, all the streamwise derivatives with the same x and z coordinates are averaged over y and only x and z dependencies are kept for all the terms of (3.1). It is important to mention that the advection term is approximated as $\mathcal{A} \approx \overline{U}(\partial k/\partial x)$ on account of $\overline{U} \gg \overline{u_2} \equiv \overline{V}, \overline{u_3} \equiv \overline{W}$. In the turbulence production ($\mathcal{P}$) and turbulent diffusion ($\mathcal{D}$) rates, the maximum contribution of terms involving a streamwise derivative is less than 5 % and 7 %, respectively. The PIV window stitching error mentioned at the start of § 3.1 is also present in figure 4 in the measurement merging regions. The discontinuity in the estimate of $\mathcal{A}$ is higher than in the $\mathcal{D}$ and $\mathcal{P}$ estimates. This could be related to the power law fitting approximation used for calculating the streamwise derivatives for $\mathcal{A}$.

https://doi.org/10.1017/jfm.2026.11161 Published online by Cambridge University Press

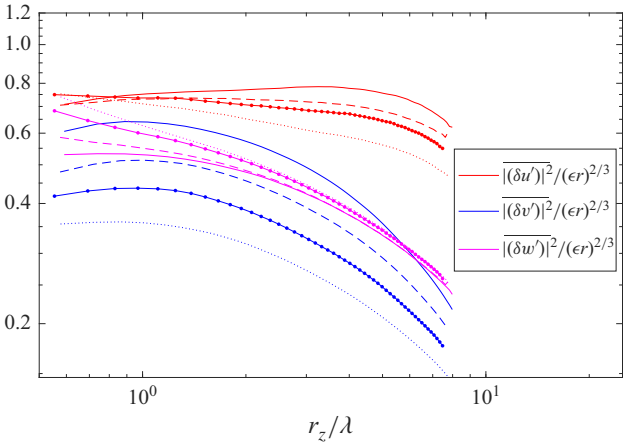


Figure 5. Compensated structure function $\overline{|\delta u'|^2}/(\epsilon r)^{2/3}$ at the centre of the field of view. The results at $x/D = 19.54$, 31.00, 40.00 and 51.60 are shown with solid, dashed, solid dotted and dotted lines, respectively.

The profiles of $\mathcal{A}$, $\mathcal{P}$ and ϵ in figure 4 are qualitatively similar to results reported in Townsend (1949) for wakes of circular cylinders, in Kewalramani *et al.* (2024) for round turbulent jets and in Cimarelli *et al.* (2021) for temporal jets. As shown in the figure where we also plot results by Uberoi & Freymuth (1970) from a sphere's axisymmetric wake for comparison, they are also qualitatively similar to profiles in axisymmetric wakes. In particular, the advection changes sign from negative to positive as z/b increases both in our slender body's turbulent wake and in the sphere's turbulent wake of Uberoi & Freymuth (1970). This change of sign reflects a change of sign in the turbulent transport/diffusion in both flows as turbulence is transported outwards by turbulence from $z = 0$ to a z of the order of b and then inwards for higher values of z. Note, however, that the advection curves for $z/b > 1$ increase with increasing x because $\overline{U}$ increases with x in that outer region (see comments on effective blockage at the start of § 3.1). In the absence of effective blockage they should be slowly decreasing in intensity like the turbulent transport/diffusion curves. The ratio $\mathcal{D}/\epsilon$ does not vary much with streamwise x as in the grid turbulence results reported by Valente & Vassilicos (2014).

3.3. *Second-order structure functions*

We close the characterisation of our prolate spheroid's wake with second-order structure functions

$$\overline{|\delta u_i'(x_j, r_k)|^2} = \frac{\overline{[u_i'(x_k + r_j) - u_i'(x_k - r_j)]^2}}{2}, \tag{3.2}$$

where the overbars indicate time averaging as in the statistics of §§ 3.1 and 3.2.

In figure 5 we plot structure functions at the centre $y = 0$, $z = 36$ mm of the PIV measurement regions. Specifically, we plot $\overline{|\delta u_1'(x,\, y = 0,\, z = 36\,\text{mm},\, r_3)|^2} \equiv \overline{|\delta u'(x,\, y = 0,\, z = 36\,\text{mm},\, r_3)|^2}$, $\overline{|\delta u_2'(x,\, y = 0,\, z = 36\,\text{mm},\, r_3)|^2} \equiv \overline{|\delta v'(x,\, y = 0,\, z = 36\,\text{mm},\, r_3)|^2}$ and $\overline{|\delta u_3'(x,\, y = 0,\, z = 36\,\text{mm},\, r_3)|^2} \equiv \overline{|\delta w'(x,\, y = 0,\, z = 36\,\text{mm},\, r_3)|^2}$, where $r_3 \equiv r_z$. We present these structure functions normalised by $(\epsilon r_z)^{2/3}$ because a turbulent flow is characterised by a 2/3 power law dependence on a two-point separation length of second-order structure functions (Pope 2000), and we plot them versus r_z/λ

https://doi.org/10.1017/jfm.2026.11161 Published online by Cambridge University Press

(where λ is the Taylor length defined as $\lambda = \sqrt{10\nu k/\epsilon}$) at every one of the four streamwise locations. Even though the local values of the Taylor length-based Reynolds number (reported in the following section) are not particularly high, an approximate $2/3$ power law scaling may be visible at $x/D = 19.54$ and $x/D = 31.00$ for the streamwise fluctuating velocity u' over a range $\lambda \leq r_z \leq 5\lambda$ with a constant of proportionality close to 0.8, which is close to the value 1 typically reported (Pope 2000). Further downstream this power law exponent seems to drop in value. No $2/3$ power law is detectable for the transverse fluctuating velocities v' and w' but the turbulence intensity is also weaker in the transverse compared with the streamwise directions. The absence of axisymmetry that characterises this nominally axisymmetric wake is also evident in these two-point statistics given that the second-order structure functions of v' and w' differ significantly. In particular, the v' structure function has a maximum at a value of r_z close to λ, which is reminiscent of results reported in Obligado & Vassilicos (2019) for decaying grid-generated turbulence, but this is not the case for the w' structure function. Note that the normalisation by ϵ of the structure functions in figure 5 has been used for convenience and not because there is any reason to expect $\epsilon^{2/3}$ scaling of these structure functions. For example, Chen & Vassilicos (2022) reported a different scaling in some turbulent wakes where evidence of self-regulating non-equilibrium was found and second-order velocity structure functions do nevertheless depend on the two-point separation length as a $2/3$ power law.

4. Spatio-temporal turbulence dissipation scalings

Self-regulating non-equilibrium means that the ratio C_ϵ^{-1} of large- to small-scale energy loss rates follow the ratio Re_λ of large- to small-scale energies so that both these ratios increase or decrease together. The variations/fluctuations of these two ratios can be either in physical space or in time and we study them here in the streamwise and transverse directions and in time.

To study how C_ϵ and Re_λ vary relative to each other, we need an estimate of large-scale energy loss rate that is proportional to the $3/2$ power of turbulent kinetic energy divided by an integral length scale. Whilst there is no fundamental ambiguity on the turbulent kinetic energy that we take to be represented by $\mathcal{U}^2 = \overline{u_i' u_i'}$, the lack of streamwise axisymmetry of the flow implies that various integral length scales can and should be considered. Following Zheng *et al.* (2023*a*) and (2023*b*), we calculate integral length scales $\mathcal{L}_{u_i}$ corresponding to velocity fluctuations u_i' as

$$\mathcal{L}_{u_i} = \int_0^{\tau_c} \rho_{u_i}(x, y, z, \tau)\overline{U}\, d\tau, \quad \rho_{u_i}(x, y, z, \tau) = \frac{\overline{u_i'(x, y, z, t)u_i'(x, y, z, t+\tau)}}{\overline{u_i'(x, y, z, t)u_i'(x, y, z, t)}}, \tag{4.1a–b}$$

where the integration is carried out up to the first zero crossing $\tau = \tau_c$ of $\rho_{u_i}(x, y, z, \tau)$, i.e. the smallest τ_c such that $\rho_{u_i}(x, y, z, \tau_c) = 0$. The Taylor frozen turbulence hypothesis is used to interpret what is effectively an integral time scale as an integral length scale. The methodology of Zheng *et al.* (2023*a*) and (2023*b*) splits the time-recorded data into many subintervals and integral scales need to be estimated for each one of these subintervals (see § 4.4). Their methodology can therefore not be applied in practice with the usual definition of the integral length scale, which involves integration over a long enough time to approximate integration to infinity. We nevertheless include a comparison between these two integral scale definitions applied to entire, non-split, time records in Appendix B.

https://doi.org/10.1017/jfm.2026.11161 Published online by Cambridge University Press

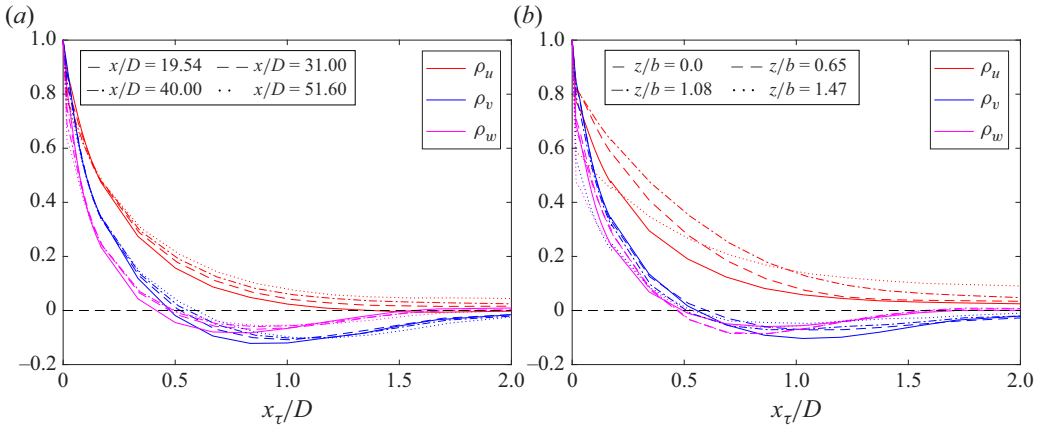


Figure 6. Variation of the velocity autocorrelations ρ_u, ρ_v and ρ_w. Panel (*a*) shows its variation with the streamwise direction at fixed $z = y = 0$. Whereas, panel (*b*) shows the z-direction variation of ρ at $x/D = 40.00$.

4.1. *Autocorrelation functions* $\rho_{u_i}(x, y, z, \tau)$

Plots of $\rho_{u_i}(x, y, z, \tau)$ versus $x_\tau/D(\equiv \overline{U}\tau/D)$ are presented in figure 6 for $i = 1, 2, 3$, i.e. for $u_1' \equiv u'$, $u_2' \equiv v'$ and $u_3' \equiv w'$, at various positions (x, y, z). Except for $x/D = 19.54$, the streamwise velocity autocorrelation $\rho_{u_1} \equiv \rho_u$ does not cross or asymptote to zero as $\overline{U}\tau/D$ grows from 0 to 2. Similar long range autocorrelations for ρ_u have previously been observed in other wakes (see Chen *et al.* 2021 and references therein). For the wake of a circular disk, Nekkanti *et al.* (2023) have attributed this behaviour to the presence of slow-moving double-helix streaky structures. Figure 6 shows that the value of ρ_u at large τ actually increases with streamwise distance. A similar increase of ρ_u can also be noted with increasing transverse z location. This behaviour may suggest streamwise elongation of streaky structures as the wake develops further along the x and z directions.

The transverse velocity autocorrelations $\rho_{u_2} \equiv \rho_v$ and $\rho_{u_3} \equiv \rho_w$ decay much faster than ρ_{u_1} with increasing $\overline{U}\tau/D$ and cross zero at all (x, y, z) positions probed; see figure 6. It is therefore possible to evaluate the integral in (4.1) for $u_2' \equiv v'$ and $u_3' \equiv w'$ and obtain the integral length scales $\mathcal{L}_{u_2} = \mathcal{L}_v$ and $\mathcal{L}_{u_3} = \mathcal{L}_w$, whereas a finite value of the integral length scale $\mathcal{L}_{u_1} = \mathcal{L}_u$ can typically not be obtained. We therefore obtain estimates of C_ϵ in terms of $\mathcal{L}_v$ and $\mathcal{L}_w$, i.e.

$$C_\epsilon^v = \frac{\epsilon \mathcal{L}_v}{\mathcal{U}^3}, \quad C_\epsilon^w = \frac{\epsilon \mathcal{L}_w}{\mathcal{U}^3}, \tag{4.2a-b}$$

and compare their spatial variations and temporal fluctuations to those of the ratio of large-scale to small-scale energies $\mathcal{U}^2/\sqrt{\nu\epsilon}$:

$$Re_\lambda = \frac{\mathcal{U}\lambda}{\nu} = \sqrt{5}\frac{\mathcal{U}^2}{\sqrt{\nu\epsilon}}. \tag{4.3}$$

In the following subsections, we study the space variations and time fluctuations of k, ϵ, $\mathcal{L}_v$, $\mathcal{L}_w$, C_ϵ^v, C_ϵ^w and Re_λ. The results for streamwise (x direction) and transverse (z direction) variations are reported in §§ 4.2 and 4.3, respectively, and those for time fluctuations are reported in § 4.4.

https://doi.org/10.1017/jfm.2026.11161 Published online by Cambridge University Press

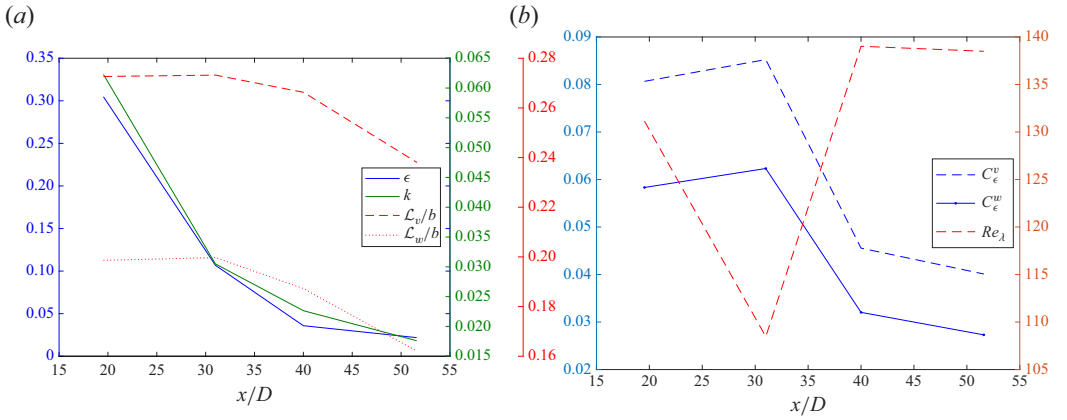


Figure 7. (*a*) Streamwise (x/D) geometric centreline ($y = z = 0$) profiles of turbulent kinetic energy (k in $m^2\ sec^{-2}$), dissipation rate (ϵ in $m^2\ sec^{-3}$) and integral length scales ($\mathcal{L}_v$ and $\mathcal{L}_w$ in m), and (*b*) streamwise centreline profiles of C_ϵ^v, C_ϵ^w and Re_λ.

4.2. *Streamwise self-regulating non-equilibrium*

The streamwise profiles of k, ϵ, $\mathcal{L}_v$, $\mathcal{L}_w$, C_ϵ^v, C_ϵ^w and Re_λ along the geometric centreline ($y = z = 0$) consist of only four points ($x/D = 19.54, 31.00, 40.00, 51.60$) and are shown in figure 7. Turbulence production is negligible on the centreline (see figure 4) and the turbulence energy and dissipation rate decay quite quickly with increasing x/D, whereas the two normalised integral scales $\mathcal{L}_v/b(x)$ and $\mathcal{L}_w/b(x)$ can be considered approximately constant at $\mathcal{L}_v/b \approx 0.25 \pm 0.02$ and $\mathcal{L}_w/b \approx 0.18 \pm 0.02$ even though they both drop at $x/D = 51.60$ because of the decrease in signal-to-noise ratio discussed in Appendix A. Following Townsend (1976) and Cafiero, Obligado & Vassilicos (2020), we may indeed expect the integral length scales to scale with the wake half-width $b(x)$.

On the other hand, C_ϵ^v, C_ϵ^w and Re_λ vary significantly from $x/D = 19.54$ to $x/D = 31.00$ and from $x/D = 31.00$ to $x/D = 40.00$ and do so in agreement with self-regulating non-equilibrium because C_ϵ^v and C_ϵ^w increase whereas Re_λ decreases from $x/D = 19.54$ to $x/D = 31.00$, and then C_ϵ^v and C_ϵ^w decrease whereas Re_λ increases from $x/D = 31.00$ to $x/D = 40.00$. The ratios $1/C_\epsilon^v$ and $1/C_\epsilon^w$ of large- to small-scale energy loss rates follow the ratio Re_λ of large- to small-scale energies and grow or decay with it. From $x/D = 40.00$ to $x/D = 51.60$, C_ϵ^v, C_ϵ^w and Re_λ do not change very significantly. Replacing $\mathcal{L}_v(x)$ by $0.25b(x)$ in the definition of C_ϵ^v and $\mathcal{L}_w(x)$ by $0.18b(x)$ in the definition of C_ϵ^w returns the near exact same plot in figure 7(*b*), suggesting that the effect of the reduced signal-to-noise ratio on the integral length scales at the further downstream x/D locations does not affect our conclusions.

This evidence of streamwise self-regulating non-equilibrium relies on only three to four centreline streamwise positions. Further evidence of self-regulating non-equilibrium in our slender body's wake is found in transverse variations and time fluctuations. This evidence is presented in the following two subsections.

4.3. *Transverse self-regulating non-equilibrium*

In figure 8 we present transverse (along z/b) profiles of integral scales $\mathcal{L}_v$ and $\mathcal{L}_w$, turbulent kinetic energy k and turbulence dissipation rate ϵ at four streamwise locations. Although the denoising method described in § 2 is used to calculate ϵ, the PIV noise in the profile of ϵ is increasingly noticeable with increasing streamwise location. This is because the signal-to-noise ratio decreases as shown in Appendix A.

https://doi.org/10.1017/jfm.2026.11161 Published online by Cambridge University Press

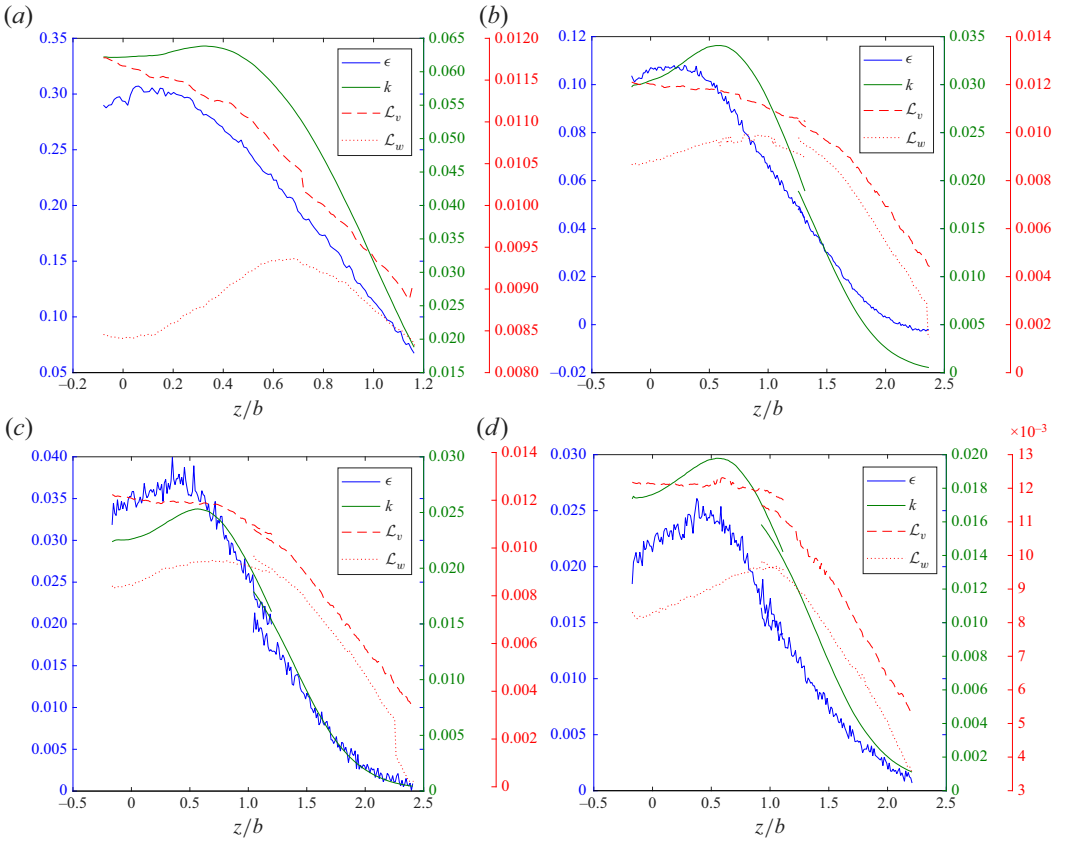


Figure 8. Profiles of $\mathcal{L}_v$, $\mathcal{L}_w$ (in m), k (in m^2 sec^{-2}) and ϵ (in m^2 sec^{-2}). The results at $x/D = 19.54$, 31.00, 40.00 and 51.60 ($y = 0$ in all cases) are shown in panels (*a–d*), respectively.

We observe $\mathcal{L}_v > \mathcal{L}_w$ and even a qualitative difference in the profiles of these two integral scales in the region $z/b \leq 0.6$ reflecting this wake's non-axisymmetry. The transverse profile of turbulent kinetic energy (k) at all four streamwise locations is qualitatively (though not quantitatively) similar to such profiles in bluff body turbulent wakes (e.g. Obligado, Dairay & Vassilicos 2016) and turbulent jets (e.g. Cafiero & Vassilicos 2019). However, the turbulence dissipation rate's transverse profile does not have its maximum value on the geometric centreline as in these flows but at a distance $z/b \approx 0.5$ off the centreline for streamwise locations $x/D = 40$ and 51.6. This is reminiscent of the numerical simulation of the turbulent wake of a 6 : 1 prolate spheroid by Ortiz-Tarin *et al.* (2021) where the maximum transverse value of the time and azimuthally averaged turbulence dissipation rate occurs at about the same transverse location.

To see whether the transverse profiles in figure 8 abide with self-regulating non-equilibrium, we need to plot transverse profiles of the non-dimensional ratios C_ϵ^v, C_ϵ^w and Re_λ. The four profiles in figure 8 (and the kinematic viscosity) hold all the necessary information for obtaining the profiles of C_ϵ^v, C_ϵ^w and Re_λ presented in figure 9. Evidence of transverse self-regulating non-equilibrium has previously been found in three qualitatively different turbulent wakes of pairs of square prisms at three different distances from each other (Chen *et al.* 2021; Alves-Portela & Vassilicos 2022). The present non-axisymmetric wake of a 6 : 1 prolate spheroid aligned with the streamwise direction is itself qualitatively different from each one of these three different wakes, yet evidence of self-regulating

https://doi.org/10.1017/jfm.2026.11161 Published online by Cambridge University Press

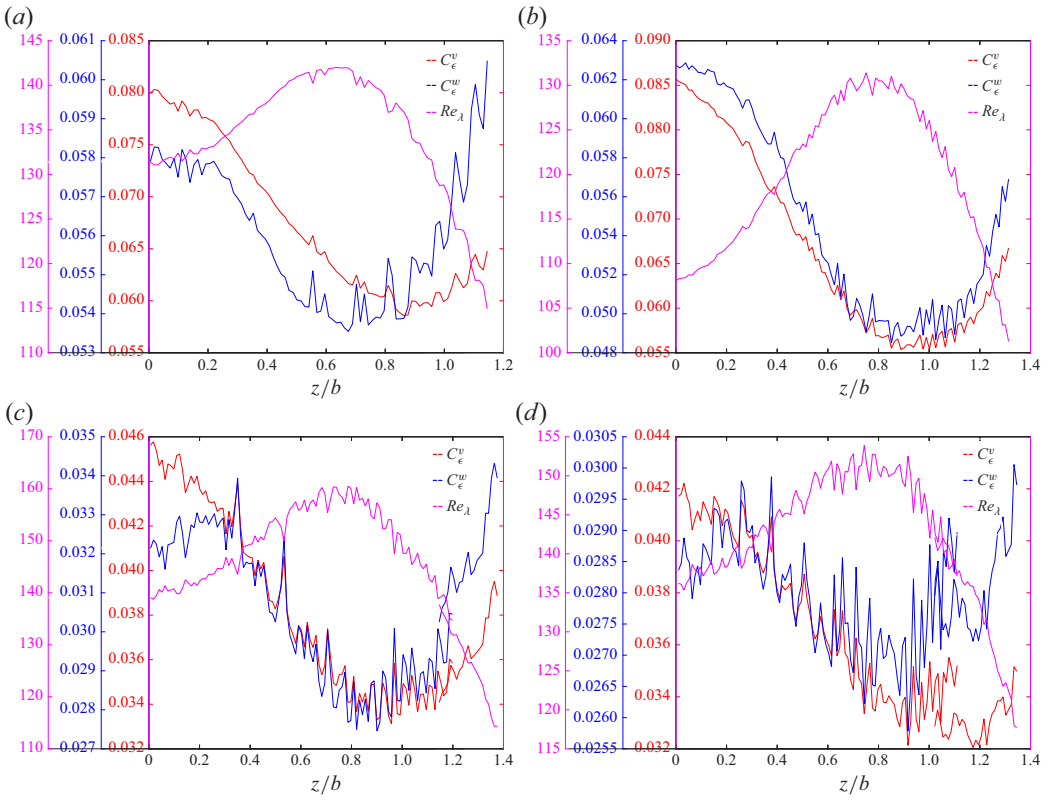


Figure 9. Transverse (z/b) profiles of C_ϵ^v, C_ϵ^w and Re_λ. Profiles at $x/D = 19.54$, 31.00, 40.00 and 51.60 (and $y = 0$ in all cases) are shown in panels (*a–d*), respectively.

non-equilibrium is found for each one of their different transverse non-homogeneities: moving along the transverse non-homogeneity of the flow, the dissipation coefficient grows when Re_λ decreases and decreases when Re_λ grows. This behaviour is also present in figure 9 where transverse profiles of C_ϵ^v, C_ϵ^w and Re_λ are shown for four different streamwise positions downstream of the 6:1 prolate spheroid: from $z/b = 0$ to about $z/b = 0.7-0.8$, C_ϵ^v decreases whereas Re_λ increases. With z/b increasing beyond $z/b = 0.8$, Re_λ decreases and C_ϵ^v increases except perhaps at our highest value of x/D where it is not clear whether C_ϵ^v increases with $z/b > 0.8$ or oscillates around a constant. These oscillations in C_ϵ^v are due to errors in our estimations of turbulence dissipation rate because the signal-to-noise ratio decreases with decreasing levels of turbulence, i.e. as x/D and z/b increase. It is, however, clearer that Re_λ decreases whereas C_ϵ^w increases with increasing z/b in the $z/b > 0.8$ regions. It is also clear that from $z/b = 0.3$ to about $z/b = 0.8$, C_ϵ^w decreases whilst Re_λ increases. Between $z/b = 0$ and $z/b = 0.3$, C_ϵ^w may be oscillating around a constant at $x/D = 19.54$, 40.00 and 51.60 (but not $x/D = 31.00$) and Re_λ does not vary much (except at $x/D = 31.00$). Whilst self-regulation may not be evident in these three near-centreline regions for C_ϵ^w, it is for C_ϵ^v.

For a different way to look at self-regulating non-equilibrium, we present two log–log plots in figure 10, one of $C_\epsilon^v Re_\lambda^2$ versus Re_λ and one of $C_\epsilon^w Re_\lambda$ versus Re_λ. The different symbols correspond to the four different streamwise distances x/D and the transverse coordinate z/b is colour coded on the symbols. Here C_ϵ^v and Re_λ seem to be related by an inverse power law $C_\epsilon^v \sim Re_\lambda^{-n}$ with n close to 2, perhaps $n \approx 1.9$, in the region from

https://doi.org/10.1017/jfm.2026.11161 Published online by Cambridge University Press

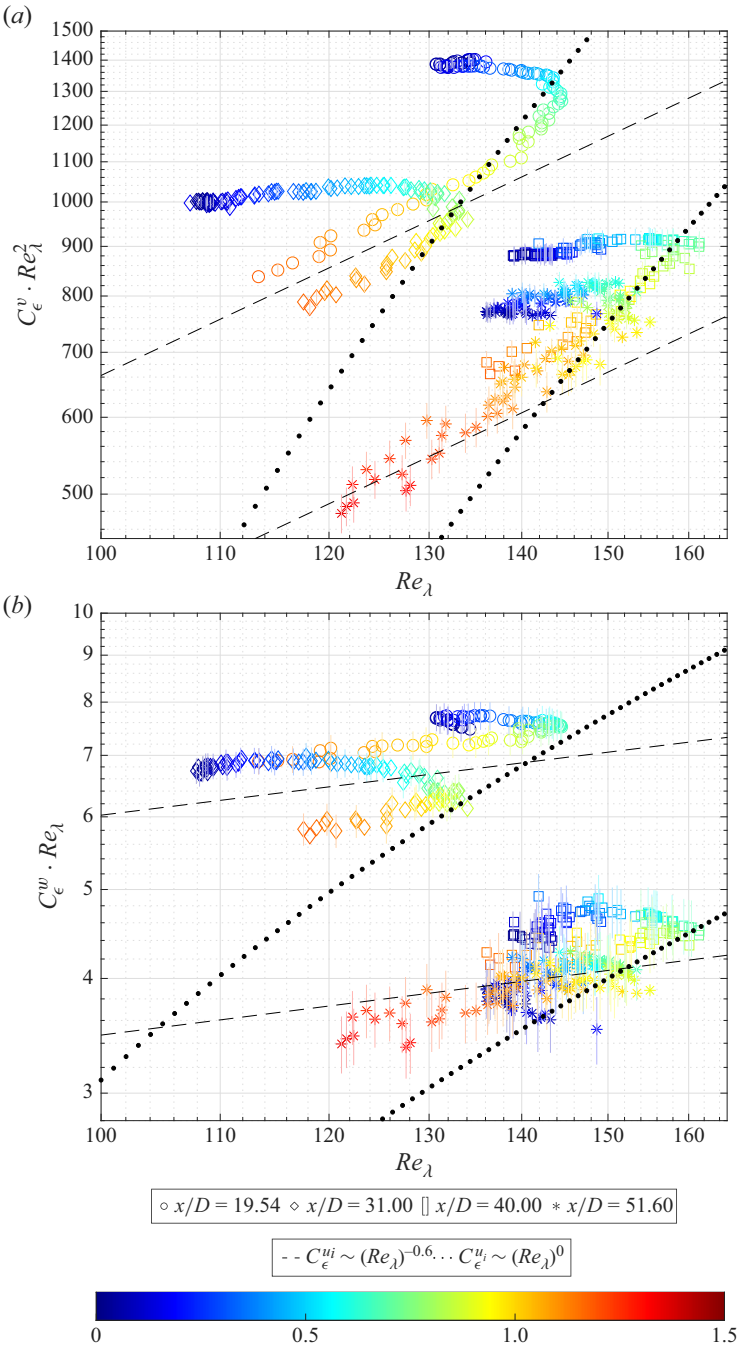


Figure 10. Self-regulating non-equilibrium scalings of C_ϵ^v and C_ϵ^w with Re_λ. (*a*) Plot of $C_\epsilon^v Re_\lambda^2$ versus Re_λ and (*b*) plot of $C_\epsilon^w Re_\lambda$ versus Re_λ. The symbols represents streamwise distance whereas their colour represents the z/b location (see the legend under the plots). Note that $y = 0$. Dash and dotted lines respectively represent scalings with $n = 0.6$ and $n = 0$ for reference (see legend under the plots). The vertical transparent lines at each data point on both plots are error bars calculated as follows: a moving average with a Gaussian smoothing function is fitted to the transverse variations of C_ϵ^v and C_ϵ^w. The maximum difference (over all transverse (z) locations) between the actual turbulence dissipation rate coefficient value and its averaged value at each streamwise location is used to define the error bar for each streamwise location.

https://doi.org/10.1017/jfm.2026.11161 Published online by Cambridge University Press

$z/b = 0$ to $z/b = 0.7$ or 0.8 for all four streamwise locations. (The exact upper limit of this z/b range is unclear. Fits of the data specifying it at different values between 0.7 and 0.8 return approximate n values ranging from 2.2 to 2.4 for $x/D = 19.54$, 1.8 to 1.9 for $x/D = 31.00$, 1.7 to 1.8 for $x/D = 40.00$ and 1.4 to 1.6 for $x/D = 51.60$.) This inverse power law quantifies the self-regulating non-equilibrium in this region but does not hold for z/b larger than 0.7 or 0.8 where self-regulation does nevertheless exist as we have seen from figure 9. A power law fit $C_\epsilon^v \sim Re_\lambda^{-n}$ in this outer region ($z/b > 0.8$) would require a much smaller positive exponent n, perhaps $n \approx 0.6$. Note however that this is the region most contaminated by low signal-to-noise ratio, particularly at the largest x/D, and where the exponent n is therefore hardest to estimate. Note also that in the transition from self-regulating non-equilibrium scaling $C_\epsilon^v \sim Re_\lambda^{-1.9}$ in the region $z/b = 0$ to 0.7 or 0.8 to self-regulating non-equilibrium scaling $C_\epsilon^v \sim Re_\lambda^{-0.6}$ in the region z/b larger than 0.8 there is a small region where Re_λ does not vary much and where C_ϵ^v may be about constant. At this stage, however, it is too early to draw any conclusions concerning this transition from one self-regulating non-equilibrium to another.

Figure 10(b) shows that an inverse relation also exists between C_ϵ^w and Re_λ in the region $z/b = 0$ to $z/b = 0.7$ or 0.8 at $x/D = 19.54$, 31.00 but it appears less well represented by a power law. At best, one might guess $C_\epsilon^w \sim Re_\lambda^{-1}$ in the region $z/b = 0$ to 0.7 or 0.8. An inverse relation between C_ϵ^w and Re_λ seems to also be present for $z/b > 0.8$ at these two streamwise stations but it is less steep, perhaps $C_\epsilon^w \sim Re_\lambda^{-0.6}$ as for C_ϵ^v. At the two further downstream stations $x/D = 40.00$, 51.60 the signal-to-noise ratio is so low, as can be seen in figure 9(c,d) for C_ϵ^w, that it is hard to draw definite conclusions from the C_ϵ^w versus Re_λ data in figure 10(b), though it may be that the data oscillate around the same self-regulating non-equilibrium scalings, i.e. $C_\epsilon^w \sim Re_\lambda^{-1}$ in the region $z/b = 0$ to 0.7 or 0.8 and $C_\epsilon^w \sim Re_\lambda^{-0.6}$ in the region $z/b = 0$ larger than 0.8. Note that, given this wake's lack of axisymmetry, the exponents n characterising the power law dependencies of C_ϵ^v and C_ϵ^w on Re_λ will change with orientation (for example, if the SPIV field of view was short in the z direction and long in the y direction unlike the present field of view, which is short in the y direction and long in the z direction).

By and large, where the signal-to-noise ratio is not too prohibitive or Re_λ variations are not too small for conclusions, a self-regulating non-equilibrium exists in the transverse profiles of C_ϵ^v, C_ϵ^w and Re_λ: where Re_λ increases C_ϵ^v and C_ϵ^w decrease and where Re_λ decreases C_ϵ^v and C_ϵ^w increase. This self-regulating behaviour has also been observed in the transverse profiles of other, qualitatively different, turbulent wakes (Chen *et al.* 2021; Alves-Portela & Vassilicos 2022) and even in some wall-normal profiles in fully developed turbulent channel flows (Apostolidis *et al.* 2022). Whereas there seems to be universality of the qualitative nature of self-regulating non-equilibrium across different non-homogeneities, quantitative differences do exist and can be easily captured when the self-regulation follows an inverse power law relation between a turbulence dissipation coefficient and Re_λ. In the present turbulent wake of a 6:1 prolate spheroid we find an approximate inverse power law $C_\epsilon^v \sim Re_\lambda^{-n}$ with $n \approx 1.9$ in the region from $z/b = 0$ to $z/b = 0.7$ or 0.8. The transverse self-regulations in the turbulent wakes of Chen *et al.* (2021) and Alves-Portela & Vassilicos (2022) also obey such an inverse power law but with n between 1.3 and 1.5.

4.4. *Temporal non-equilibrium scaling*

Rather than examine how Re_λ and turbulence dissipation coefficients vary with streamwise and spanwise directions in physical space, Zheng *et al.* (2023*a*) and (2023*b*) introduced a methodology for studying their time fluctuations at a given spatial location. They applied

https://doi.org/10.1017/jfm.2026.11161 Published online by Cambridge University Press

their methodology to grid-generated turbulence and obtained the interesting results concerning self-regulating non-equilibrium that we described in the introduction. In this subsection we apply their methodology to the turbulent wake of our 6:1 prolate spheroid with the principal axis aligned with the streamwise direction and study the time fluctuations of the Taylor length-based Reynolds number and turbulence dissipation coefficients at various positions $(x,\, y = 0,\, z)$

Data recorded in time at a given spatial position are therefore divided into consecutive intervals of time duration $\mathcal{T}$. Each one of these intervals is identified by the time t_i at the centre of the interval, where i varies from 1 to N, the ratio of the total measurement time to $\mathcal{T}$. Integral length scales $\mathcal{L}_v^{t_i}$ and $\mathcal{L}_w^{t_i}$, velocity scales $\mathcal{U}^{t_i}$ (equal to the square root of twice the turbulent kinetic energy averaged over the interval) and turbulent dissipation rates ϵ^{t_i} are calculated for each one of these time intervals. The time intervals are long enough to ensure that autocorrelation functions $\rho_v^{t_i}$ and $\rho_w^{t_i}$ calculated using data only from the time interval labelled t_i have a zero crossing. Integral scales $\mathcal{L}_v^{t_i}$ and $\mathcal{L}_w^{t_i}$ can then be calculated by integrating (up to the first zero crossing) the autocorrelation functions $\rho_v^{t_i}$ and $\rho_w^{t_i}$ of fluctuating velocity components v' and w', respectively. We verified that an interval time duration of 20 eddy turnover times, i.e. $\mathcal{T} = 20\mathcal{L}_v/\mathcal{U}$, is sufficient to ensure the presence of zero crossings in all the autocorrelation functions $\rho_v^{t_i}$ and $\rho_w^{t_i}$ and consequent unambiguous calculation of the integral scales $\mathcal{L}_v^{t_i}$ and $\mathcal{L}_w^{t_i}$. We also tried interval time durations $\mathcal{T}$ larger than $20\mathcal{L}_v/\mathcal{U}$, up to $\mathcal{T} = 50\mathcal{L}_v/\mathcal{U}$, and confirmed that all our conclusions in this subsection remain the same.

On the basis of $\mathcal{L}_v^{t_i}$, $\mathcal{L}_w^{t_i}$, $\mathcal{U}^{t_i}$ and ϵ^{t_i} we calculate turbulence dissipation coefficients $C_\epsilon^{t_i,v} \equiv \epsilon^{t_i}\mathcal{L}_v^{t_i}/(\mathcal{U}^{t_i})^3$, $C_\epsilon^{t_i,w} \equiv \epsilon^{t_i}\mathcal{L}_w^{t_i}/(\mathcal{U}^{t_i})^3$ and Reynolds numbers $Re_\lambda^{t_i} \equiv \sqrt{5}(\mathcal{U}^{t_i})^2/\sqrt{\nu\epsilon^{t_i}}$ for each t_i, i.e. for each time interval labelled t_i. The ratios $C_\epsilon^{t_i,v}$, $C_\epsilon^{t_i,w}$ and $Re_\lambda^{t_i}$ are functions of x, z and t_i whereas the ratios C_ϵ^{v}, C_ϵ^{w} and Re_λ are functions of x and z only ($y = 0$ in all cases). The quantities most contaminated by noise are (by far) the turbulence dissipation rates. However, they are all statistically well converged within each time interval. Hence, the signal-to-noise ratio can be expected to be the same for ϵ^{t_i} (turbulence dissipation rate averaged over time in the time interval labelled t_i) and for ϵ (turbulence dissipation rate averaged over the entire time record). For an estimate of the noise in the normalised dissipation ratio ϵ^{t_i}/ϵ, we decompose the turbulent dissipation rates as $\epsilon \equiv \epsilon^T + \epsilon^N$ and $\epsilon^{t_i} \equiv \epsilon^{t_i,T} + \epsilon^{t_i,N}$, where the symbols with superscript T denote the true value of the dissipation and with superscript N denote the noise associated with the PIV measurements of dissipation. Using this decompositon, the ratio ϵ^{t_i}/ϵ becomes

$$\begin{aligned}\frac{\epsilon^{t_i}}{\epsilon} &= \frac{\epsilon^{t_i,T}}{\epsilon^T}\left(\frac{1+\frac{\epsilon^{t_i,N}}{\epsilon^{t_i,T}}}{1+\frac{\epsilon^N}{\epsilon^T}}\right) \approx \frac{\epsilon^{t_i,T}}{\epsilon^T}\left[\left(1+\frac{\epsilon^{t_i,N}}{\epsilon^{t_i,T}}\right)\left(1-\frac{\epsilon^N}{\epsilon^T}\right)\right] \\ &\approx \frac{\epsilon^{t_i,T}}{\epsilon^T}\left(1+\frac{\epsilon^{t_i,N}}{\epsilon^{t_i,T}}-\frac{\epsilon^N}{\epsilon^T}-\frac{\epsilon^{t_i,N}}{\epsilon^{t_i,T}}\frac{\epsilon^N}{\epsilon^T}\right). \end{aligned} \tag{4.4}$$

The signal-to-noise ratio being the same for ϵ^{t_i} and ϵ, we have $\epsilon^{t,N}/\epsilon^{t,T} \approx \epsilon^N/\epsilon^T$, which, using (4.4), implies that

$$\frac{\epsilon^{t_i}}{\epsilon} \approx \frac{\epsilon^{t_i,T}}{\epsilon^T}\left(1-\left(\frac{\epsilon^N}{\epsilon^T}\right)^2\right). \tag{4.5}$$

As a result, if the noise is decorrelated from the signal and if the parts of ϵ and ϵ^{t_i} due to noise are, say, 40 % of their value without noise, the part of ϵ^{t_i}/ϵ due to noise will only

https://doi.org/10.1017/jfm.2026.11161 Published online by Cambridge University Press

be 16 % (second-order contamination given by the square of 40 %) of the value of ϵ^{t_i}/ϵ without noise. We therefore chose to plot $C_\epsilon^{t_i,v}/C_\epsilon^v$, $C_\epsilon^{t_i,w}/C_\epsilon^w$ and $Re_\lambda^{t_i}/Re_\lambda$ in order to reduce the effect of dissipation noise.

Temporal fluctuations of $C_\epsilon^{t_i,v}/C_\epsilon^v$, $C_\epsilon^{t_i,w}/C_\epsilon^w$ and $Re_\lambda^{t_i}/Re_\lambda$, i.e. versus t_i, are plotted in the left-hand column of figures 11 and 12 for our four different streamwise locations very close to the geometric centreline, namely $y=0$, $z/b=0.01$. Anticorrelations in the time (t_i) fluctuations of $C_\epsilon^{t_i,v}/C_\epsilon^v$ and $Re_\lambda^{t_i}/Re_\lambda$ (figure 11) and in the time fluctuations of $C_\epsilon^{t_i,w}/C_\epsilon^w$ and $Re_\lambda^{t_i}/Re_\lambda$ (figure 12) become increasingly evident as x/D increases. In fact, $C_\epsilon^{t_i,v}/C_\epsilon^v$, $C_\epsilon^{t_i,w}/C_\epsilon^w$ and $Re_\lambda^{t_i}/Re_\lambda$ do not vary much in time at $x/D=19.54$; the anticorrelations appear as $C_\epsilon^{t_i,v}/C_\epsilon^v$, $C_\epsilon^{t_i,w}/C_\epsilon^w$ and $Re_\lambda^{t_i}/Re_\lambda$ fluctuate over an increasingly wide range of values with increasing x/D. This anticorrelation gets increasingly well defined as x/D increases, and the scatter plots on the right-hand column of figures 11 and 12 show that it tends to be expressed by fairly well-defined power laws $C_\epsilon^{t_i,v}/C_\epsilon^v \sim (Re_\lambda^{t_i}/Re_\lambda)^{-1.8}$ and $C_\epsilon^{t_i,w}/C_\epsilon^w \sim (Re_\lambda^{t_i}/Re_\lambda)^{-1.8}$ with increasing x/D.

We now move beyond the centreline and look at temporal fluctuations of $C_\epsilon^{t_i,v}/C_\epsilon^v$, $C_\epsilon^{t_i,w}/C_\epsilon^w$ and $Re_\lambda^{t_i}/Re_\lambda$ at various transverse locations z/b ($y=0$) for each one of the four streamwise positions x/D. We present scatter plots of $C_\epsilon^{t_i,v}/C_\epsilon^v$ versus $Re_\lambda^{t_i}/Re_\lambda$ in figure 13 and scatter plots of $C_\epsilon^{t_i,w}/C_\epsilon^w$ versus $Re_\lambda^{t_i}/Re_\lambda$ in figure 14. Anticorrelations between fluctuations of $C_\epsilon^{t_i,v}/C_\epsilon^v$ and $Re_\lambda^{t_i}/Re_\lambda$ (figure 13) and between fluctuations of $C_\epsilon^{t_i,w}/C_\epsilon^w$ and $Re_\lambda^{t_i}/Re_\lambda$ (figure 14) appear with increasing clarity as x/D increases for every z/b. Indeed, for every z/b, these anticorrelations tend to be represented by well-defined power laws close to $C_\epsilon^{t_i,v}/C_\epsilon^v \sim (Re_\lambda^{t_i}/Re_\lambda)^{-1.9}$ and $C_\epsilon^{t_i,w}/C_\epsilon^w \sim (Re_\lambda^{t_i}/Re_\lambda)^{-1.9}$ as x/D increases.

We have already noted that $C_\epsilon^{t_i,v}/C_\epsilon^v$, $C_\epsilon^{t_i,w}/C_\epsilon^w$ and $Re_\lambda^{t_i}/Re_\lambda$ do not vary much in time at $x/D=19.54$ near the centreline (figures 11 and 12); we now observe that they do not vary much in time off the centreline either at $x/D=19.54$; see plots for $x/D=19.54$ and various values of z/b in figures 13 and 14. With increasing x/D, the fluctuations of $C_\epsilon^{t_i,v}/C_\epsilon^v$, $C_\epsilon^{t_i,w}/C_\epsilon^w$ and $Re_\lambda^{t_i}/Re_\lambda$ occur over an increasing range of values for any z/b, and the anticorrelations appear increasingly clearly as this range grows.

It is hard not to notice that the exponent $n \approx 1.9$ is nearly the same for the power laws $C_\epsilon^{t_i,v}/C_\epsilon^v \sim (Re_\lambda^{t_i}/Re_\lambda)^{-n}$ and $C_\epsilon^{t_i,w}/C_\epsilon^w \sim (Re_\lambda^{t_i}/Re_\lambda)^{-n}$, encoding self-regulation in time at high enough x/D and for the power law $C_\epsilon^v \sim Re_\lambda^{-n}$, encoding transverse self-regulation from $z/b=0$ to $z/b=0.7$ or 0.8. However, the transverse self-regulations of C_ϵ^v at higher values of z/b and of C_ϵ^w are different.

5. Conclusion

The turbulent wake of a 6:1 prolate spheroid with its principal axis aligned with the incoming non-turbulent flow is a very different turbulent wake from bluff body wakes, not least because it is not axisymmetric even though it nominally is (see Williams & Smits 2024). Our SPIV measurements have identified this asymmetry and have documented the non-homogeneity of our slender body's turbulent wake. Unlike turbulent bluff body wakes and turbulent jets, the transverse turbulence dissipation profile has its maximum away from the geometric centreline. The structure function of the streamwise fluctuating velocity component varies approximately as the 2/3 power law of the two-point transverse separation distance over a significant range, suggesting that the Reynolds number is high enough in these particular conditions for the flow to have developed some kind of turbulence characteristics.

https://doi.org/10.1017/jfm.2026.11161 Published online by Cambridge University Press

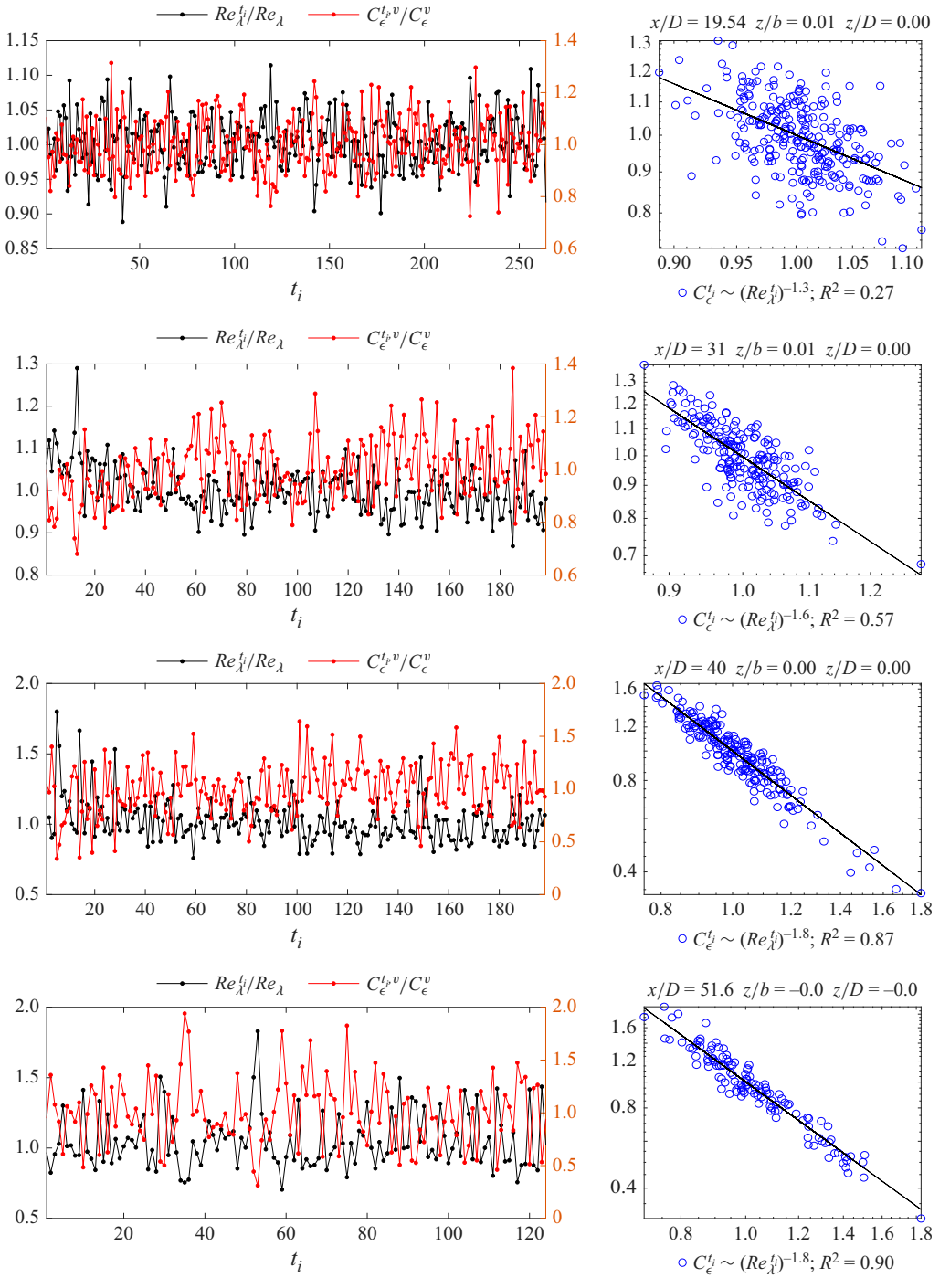


Figure 11. Temporal fluctuations very near or on the geometric centreline ($y = z \approx 0$). Here $C_\epsilon^{t_i,v}$ and $Re_\lambda^{t_i}$ fluctuations along time t_i are shown in the plots on the left column. The plots on the right column are log–log scatter plots of $C_\epsilon^{t_i,v}/C_\epsilon^v$ (vertical axis) versus $Re_\lambda^{t_i}/Re_\lambda$ (horizontal axis) and the straight lines on these plots are best fit power laws $C_\epsilon^{t_i,v}/C_\epsilon^v \sim (Re_\lambda^{t_i}/Re_\lambda)^{-n}$. The exponents n and the coefficients of determination R^2 indicating the quality of the power law fit are given at the bottom of each right column plot. The streamwise location increases from the top to bottom row.

https://doi.org/10.1017/jfm.2026.11161 Published online by Cambridge University Press

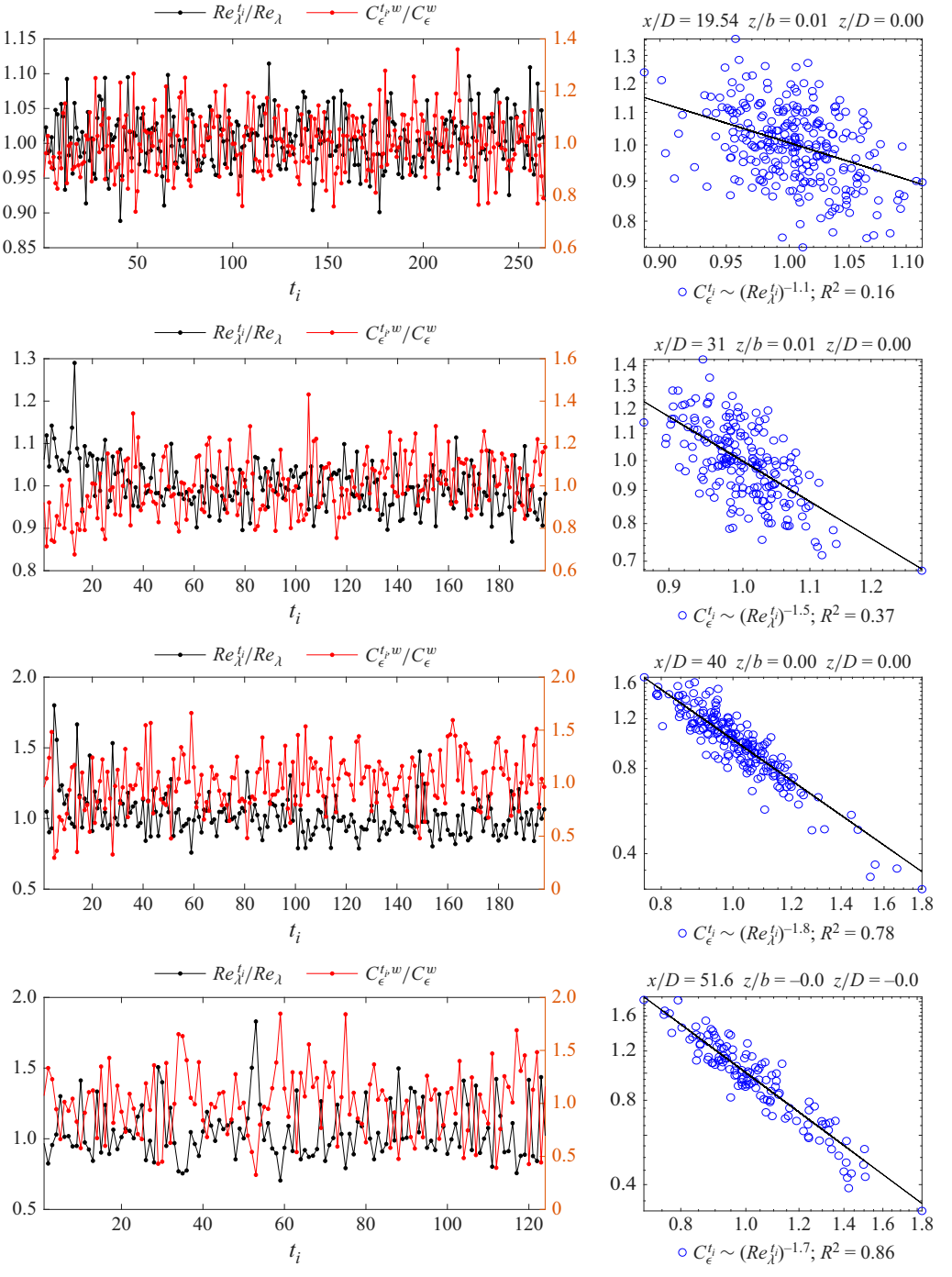


Figure 12. Temporal fluctuations very near or on the geometric centreline ($y = z \approx 0$). Here $C_\epsilon^{t_i,w}$ and $Re_\lambda^{t_i}$ fluctuations along time t_i are shown in the plots on the left column. The plots on the right column are log–log scatter plots of $C_\epsilon^{t_i,w}/C_\epsilon^w$ (vertical axis) versus $Re_\lambda^{t_i}/Re_\lambda$ (horizontal axis) and the straight lines on these plots are best fit power laws $C_\epsilon^{t_i,w}/C_\epsilon^w \sim (Re_\lambda^{t_i}/Re_\lambda)^{-n}$. The exponents n and the coefficients of determination R^2 indicating the quality of the power law fit are given at the bottom of each right column plot. The streamwise location increases from the top to bottom row.

https://doi.org/10.1017/jfm.2026.11161 Published online by Cambridge University Press

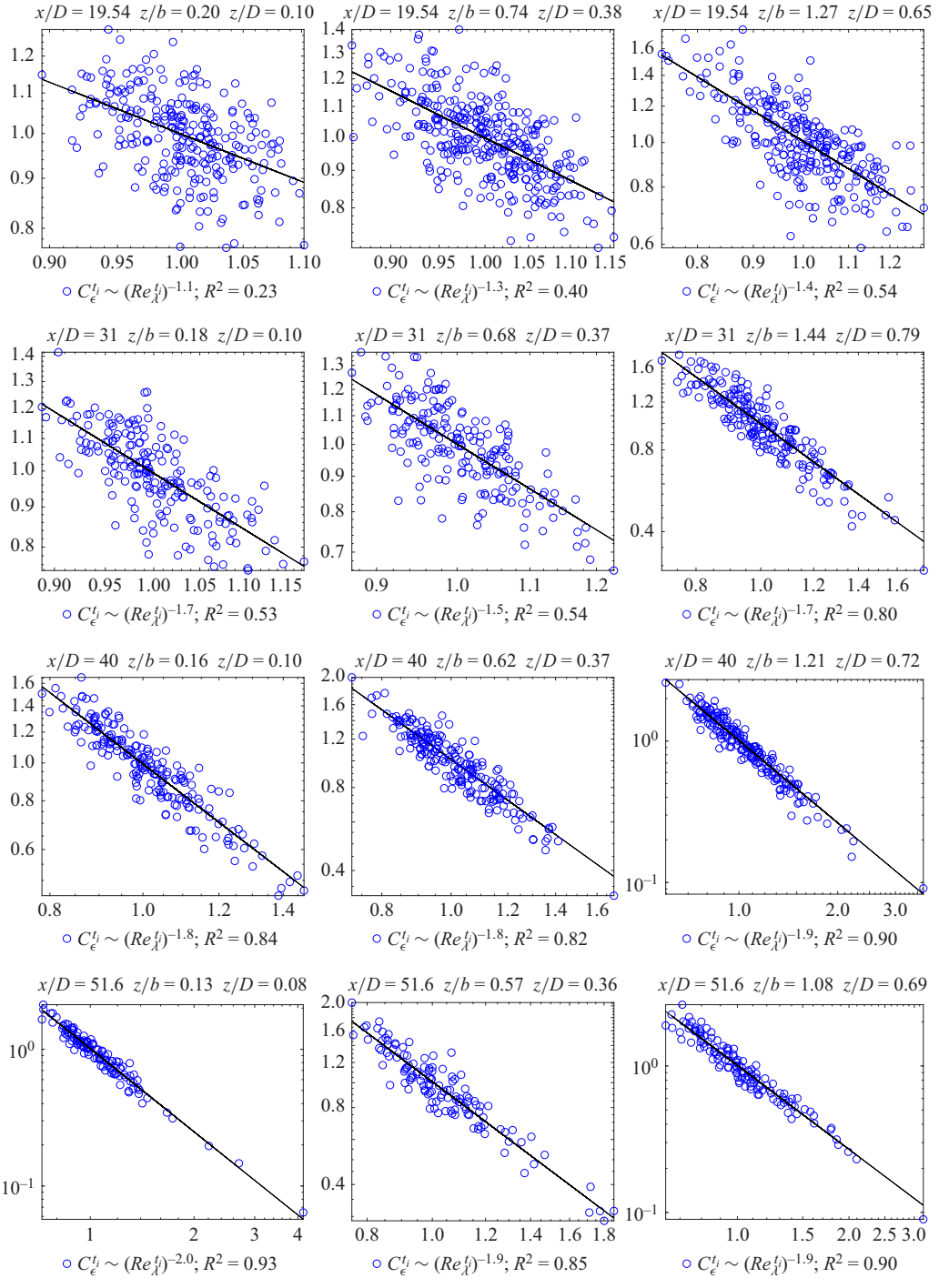


Figure 13. Log–log scatter plots of $C_\epsilon^{t_i,v}/C_\epsilon^v$ (vertical axis) versus $Re_\lambda^{t_i}/Re_\lambda$ (horizontal axis). The straight lines on these plots are best fit power laws $C_\epsilon^{t_i,v}/C_\epsilon^v \sim (Re_\lambda^{t_i}/Re_\lambda)^{-n}$. The exponents n and the coefficients of determination R^2 indicating the quality of the power law fit are given at the bottom of each plot. Each plot corresponds to a position x/D, $y = 0$, z/b, z/D as indicated at the top of the plot. Streamwise position x/D increases from top to bottom rows and the transverse position z/b increases from left to right columns.

https://doi.org/10.1017/jfm.2026.11161 Published online by Cambridge University Press

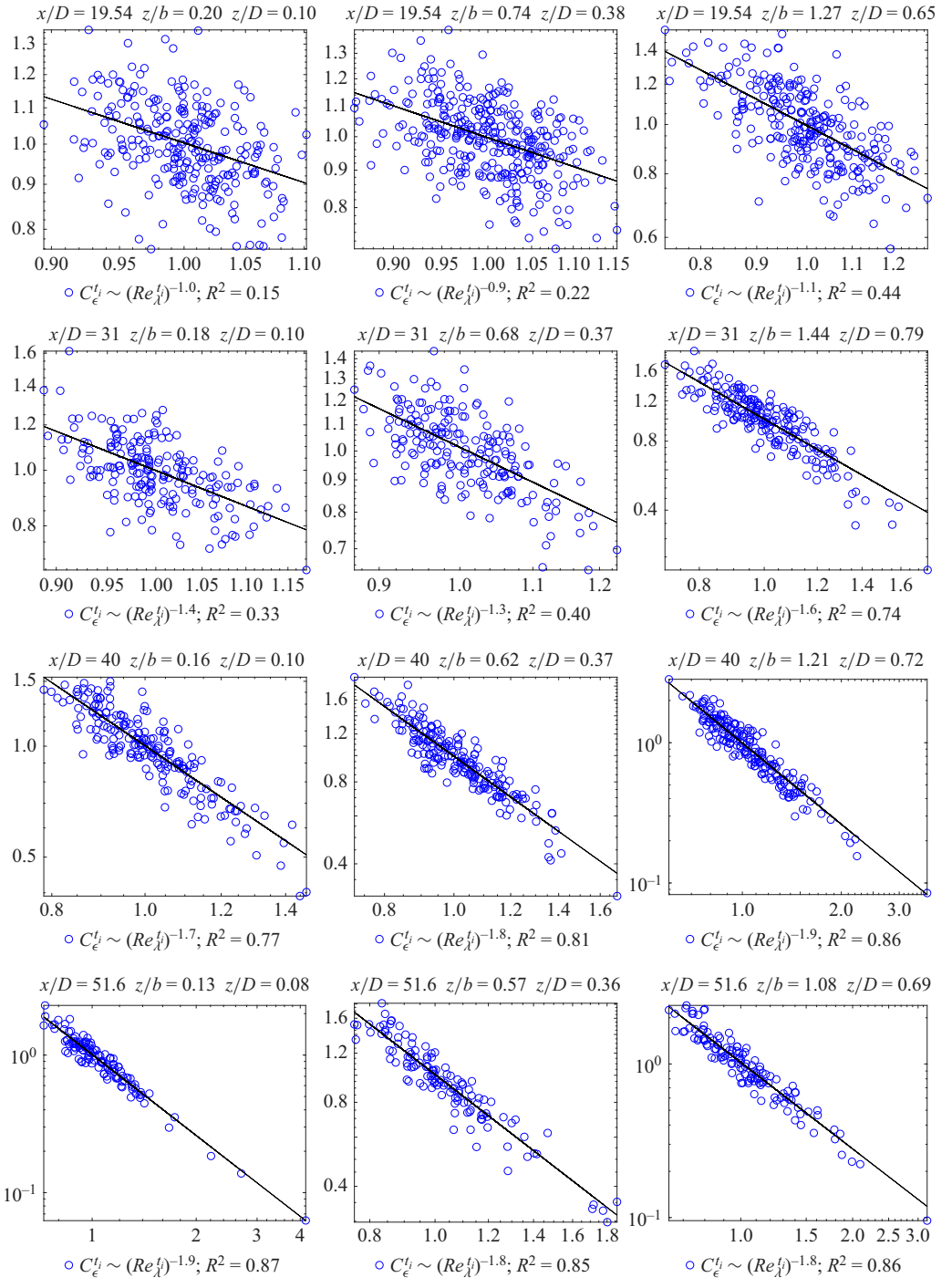


Figure 14. Log–log scatter plots of $C_\epsilon^{t_i,w}/C_\epsilon^{w}$ (vertical axis) versus $Re_\lambda^{t_i}/Re_\lambda$ (horizontal axis). The straight lines on these plots are best fit power laws $C_\epsilon^{t_i,w}/C_\epsilon^{w} \sim (Re_\lambda^{t_i}/Re_\lambda)^{-n}$. The exponents n and the coefficients of determination R^2 indicating the quality of the power law fit are given at the bottom of each plot. Each plot corresponds to a position x/D, $y = 0$, z/b, z/D as indicated at the top of the plot. Streamwise position x/D increases from top to bottom rows and the transverse position z/b increases from left to right columns.

https://doi.org/10.1017/jfm.2026.11161 Published online by Cambridge University Press

We have defined two turbulence dissipation coefficients in terms of two integral length scales, one for each transverse fluctuating velocity v' and w'. By long time averaging we have obtained two turbulence dissipation coefficients C_ϵ^v, C_ϵ^w and an energy ratio Re_λ as functions of streamwise and transverse coordinates x and z. By applying the methodology of Zheng *et al.* (2023*a*) and (2023*b*) and averaging over shorter time intervals centred at times t_i, we have obtained two turbulence dissipation coefficients $C_\epsilon^{t_i,v}$, $C_\epsilon^{t_i,w}$ and an energy ratio $Re_\lambda^{t_i}$ as functions of x, z and time t_i. We have observed self-regulating non-equilibrium in transverse non-homogeneity wherever the transverse spatial variations of C_ϵ^v and Re_λ or C_ϵ^w and Re_λ are large enough; and we have also observed self-regulating non-equilibrium in time t_i wherever the time fluctuations of $C_\epsilon^{t_i,v}$ and $Re_\lambda^{t_i}$ or $C_\epsilon^{t_i,w}$ and $Re_\lambda^{t_i}$ are of high enough amplitude. In fact, the amplitude of these fluctuations increases with x/D and self-regulating non-equilibrium in time becomes increasingly well defined. As x/D increases, these fluctuations fall increasingly sharply on $C_\epsilon^{t_i,v}/C_\epsilon^v \sim (Re_\lambda^{t_i}/Re_\lambda)^{-n}$ and $C_\epsilon^{t_i,w}/C_\epsilon^w \sim (Re_\lambda^{t_i}/Re_\lambda)^{-n}$ with the same exponent $n \approx 1.9$ for any z/b.

The transverse profiles of C_ϵ^v, C_ϵ^w and Re_λ also abide with self-regulating non-equilibrium as C_ϵ^v and C_ϵ^w increase/decrease where Re_λ decreases/increases. Whilst the transverse self-regulations of C_ϵ^v at $z/b > 0.8$ and of C_ϵ^w throughout z are different from those of C_ϵ^v in the range $z/b = 0$ to $z/b = 0.7$ or 0.8 (see § 4.3 for details), the transverse profiles of C_ϵ^v and Re_λ from $z/b = 0$ to $z/b = 0.7$ or 0.8 obey $C_\epsilon^v \sim Re_\lambda^{-n}$ with the same exponent $n \approx 1.9$ for time fluctuations. This echoes the findings of Zheng *et al.* (2023*a*) and (2023*b*) in very different turbulent flows, active and regular grid-generated turbulence, where the time fluctuations of the Taylor length-based Reynolds number and the turbulence dissipation coefficient follow the same scaling law that is obeyed by streamwise variations of the Taylor length-based Reynolds number and turbulence dissipation coefficient upstream of the far field in regular grid-generated turbulence (see the fifth paragraph of the introduction). However, whereas the scaling law reported by Zheng *et al.* (2023*a*) and (2023*b*) falls within a universality class of self-regulating non-equilibrium that includes planar jets, axisymmetric wakes, grid-generated turbulence, freely decaying turbulence and fluctuating forced homogeneous/periodic turbulence (see the second paragraph of the introduction), the scaling laws $C_\epsilon^{t_i,v}/C_\epsilon^v \sim (Re_\lambda^{t_i}/Re_\lambda)^{-1.9}$ and $C_\epsilon^{t_i,w}/C_\epsilon^w \sim (Re_\lambda^{t_i}/Re_\lambda)^{-1.9}$ reported here for time fluctuations in the turbulent wake of a 6:1 prolate spheroid are different from any previously reported self-regulating non-equilibrium scaling. The present slender body's turbulent wake is different enough in terms of non-homogeneity and symmetry breaking to warrant its own, different, power law relation between the ratio of large- to small-scale energy loss rates and the ratio of large- to small-scale energies. Even so, it does not escape self-regulating non-equilibrium qualitatively and adds to the evidence that self-regulating non-equilibrium may be universal across a wide range of non-homogeneities and non-stationarities.

One may ask whether Kolmogorov scale-by-scale equilibrium is eventually achieved either downstream for a given global Reynolds number or in this paper's range of x/D locations as the global Reynolds number increases. Kolmogorov scale-by-scale equilibrium is a high-Reynolds-number behaviour. Just on this account, there is no reason for it to appear as the local Reynolds number decreases with increasing downstream distance. As the global Reynolds number increases, the recent theory of turbulence cascades in non-homogeneous turbulence with weak turbulence production by Chen & Vassilicos (2022) and Beaumard *et al.* (2024) predicts that the cascade remains non-Kolmogorov throughout the inertial range. We therefore expect self-regulating

https://doi.org/10.1017/jfm.2026.11161 Published online by Cambridge University Press

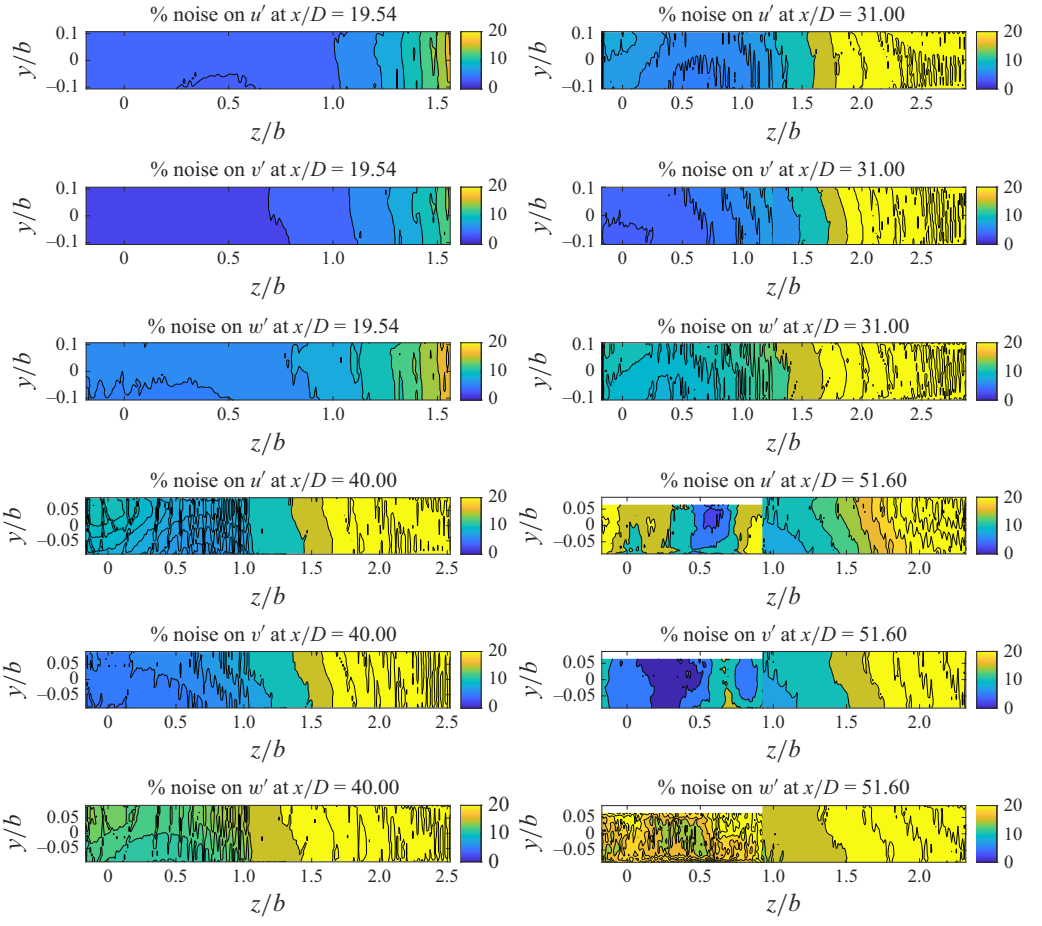


Figure 15. Percentage of PIV noise in u', v' and w' fluctuating velocities and at streamwise locations $x/D =$ 19.45, 31.00, 40.00 and 51.60. The information about the velocity and streamwise location for each figure is in its title above.

non-equilibrium to persist with increasing global Reynolds numbers at the positions where it has been detected here.

Funding. We acknowledge funding by the European Union (ERC Advanced Grant NoStaHo, project number 101054117). Views and opinions expressed are, however, those of the author(s) only and do not necessarily reflect those of the European Union or the European Research Council. Neither the European Union nor the granting authority can be held responsible for them. The equipment used in this work is funded under the project Recherche et Innovation en Transports et Mobilité Eco-responsables et Autonomes (RITMEA) CPER 2021-2027 (and previously CISIT then Elsat2020), co-funded by the European Regional Development Fund, the French state and FEDER Hauts-de-France Regional Council.

Declaration of interests. The authors report no conflict of interest.

Data availability statement. The data in the present manuscript will be made available upon request.

Appendix A. Noise in the SPIV measurements

A major source of noise in turbulent fluctuating velocity measurements with PIV results from the approximation of the location of seeding particles in the pixelated images.

https://doi.org/10.1017/jfm.2026.11161 Published online by Cambridge University Press

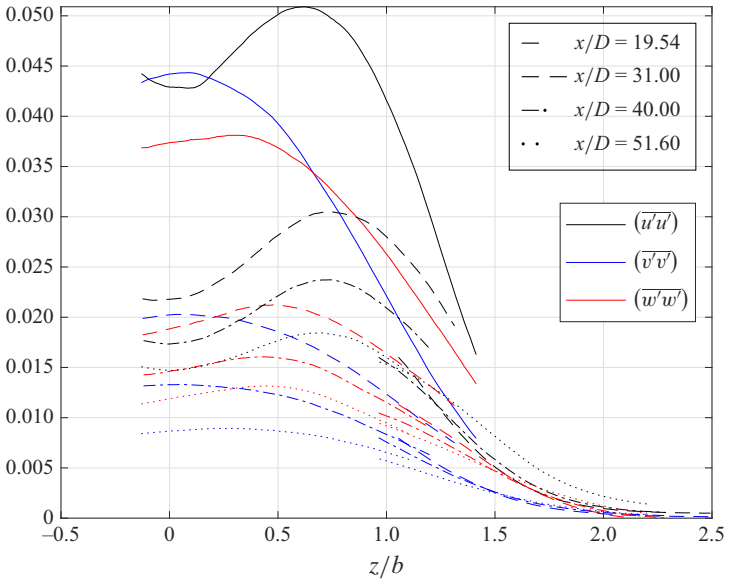


Figure 16. Transverse profiles of the normal stresses $\overline{u_i' u_i'}$ for $u_1' \equiv u'$ $(i = 1)$, $u_2' \equiv v'$ $(i = 2)$ and $u_3' \equiv w'$ $(i = 3)$.

Fluctuating velocities at two consecutive IWs (separated by a small multiple of η_k) are highly correlated. However, noise in the fluctuating velocity caused by the aforementioned pixelisation decorrelates with spatial separation. Due to this rapid noise decorrelation at small spatial distances, the magnitude of the error related to u_i' can be estimated using the autocorrelation $\overline{u_i' u_i'}$ in the following way: the percentage of noise related to u_i' at any y, z location in the field of view is calculated by comparing the difference between $\overline{u_i'(y, z) u_i'(y, z)}$ and $\overline{u_i'(y, z) u_i'(y', z)}$ for y' and y being adjacent vector spacings in the y direction. We use the separation in y rather than in z because the IW size in the y direction (δy) is the smallest as mentioned in table 1. In figure 15 we plot $100 \times (\overline{u_i'(y, z) u_i'(y, z)} - \overline{u_i'(y, z) u_i'(y', z)}) / \overline{u_i'(y, z) u_i'(y', z)}$ as a measure of the percentage noise contaminating u_i' for each $i = 1, 2, 3$ and at each one of the four streamwise positions $x/D = 19.51$, 31.00, 40.00 and 51.60.

The PIV field in the y direction is not long enough for variations in percentage noise contamination to be significant, but it is in the z direction. For all fluctuating velocities $(u_i' \equiv u', v', w')$ at all four streamwise positions, there is a gradual decrease or constancy followed by an increase in percentage noise in the z direction such that the minimum percentage noise occurs invariably in the region $0 < z/b < 0.6$. Additionally, the percentage error at any transverse location increases with the streamwise position. As can be seen in figure 16, this increase in noise contamination is correlated with the decrease with x/D in magnitude of normal turbulent stresses $\overline{u_i' u_i'}$ for all $i = 1, 2, 3$. In PIV measurements, noise is typically a fraction of a pixel's displacement. As $\overline{u_i' u_i'}$ decreases with increasing x/D or z/b, the signal-to-noise ratio can decrease. This is confirmed here by the presence of more than 20 % noise in the very low turbulent fluctuation region $z/b > 2$. At the geometric centre $y = z = 0$ where the HWA data were taken, the noise in u' (accessed by our HWA) exceeds 10 % at $x/D = 40.00$ and $x/D = 51.60$, but is well below 10 % as shown in figure 15. Furthermore, it can also be observed that the noise

https://doi.org/10.1017/jfm.2026.11161 Published online by Cambridge University Press

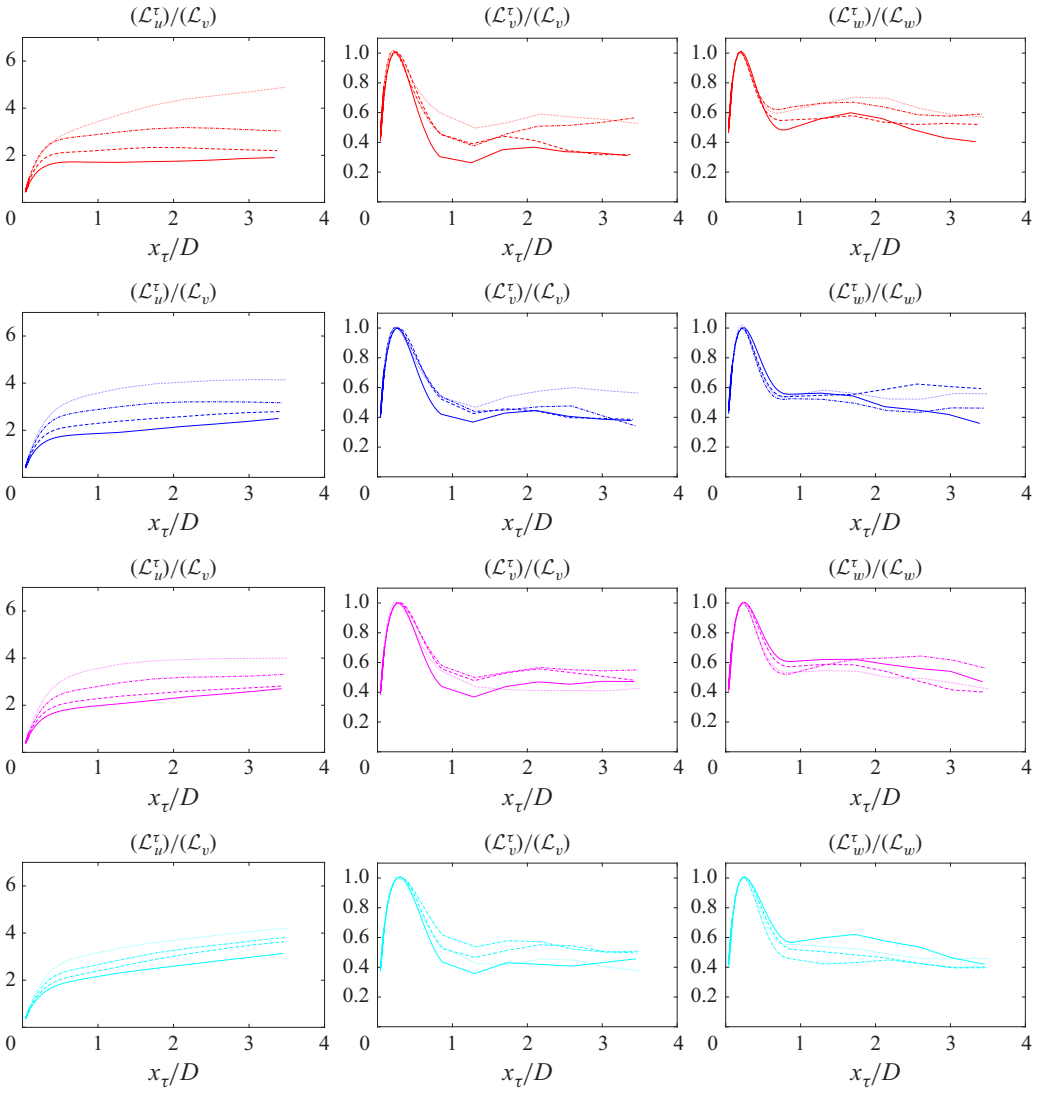


Figure 17. Variation with x_τ/D (horizontal axis for all plots) of the integral length scale ratios $\mathcal{L}_u^\tau/\mathcal{L}_v$ (left column), $\mathcal{L}_v^\tau/\mathcal{L}_v$ (middle column) and $\mathcal{L}_w^\tau/\mathcal{L}_w$ (right column) obtained by integrating autocorrelation functions up to τ. The red (first row), blue (second row), magenta (third row) and cyan (fourth row) colour lines are used to show the results at $x/D = 19.54$, 31.00, 40,00 and 51.6, respectively. The solid(−), dashed (--), dashed-doted ($\cdot-$) and dotted ($\cdot s$) lines are used to show the results at $z/D = 0.00$, 0.26, 0.5 and 0.75, respectively.

contamination in v' is less than u' and w'. This may be due to a difference in the condition of two lasers (each operating at 7 kHz), which may give a bias and, hence, higher error in the reconstructed velocity in the Soloff method.

Although with increasing temporal separation the noise in the fluctuating velocities decorrelates faster than the signal (i.e. the actual fluctuating velocity), it remains finite. This may be due to particle overlap in the IWs. As shown in figure 15, a higher noise-to-signal ratio ($> 10\,\%$) exists for u' at $x/D = 40.00$ and 51.6, and for w' at $x/D = 31.00$, 40.00 and 51.6. This higher noise-to-signal ratio is due to their lower magnitudes. In these locations with lower velocity fluctuations, the finite correlation of noise at $n = 1$ separation

https://doi.org/10.1017/jfm.2026.11161 Published online by Cambridge University Press

appears significant to effect correct ϵ_{iso1} estimation at $x/D = 40.00$ and 51.6 and ϵ_{iso2} estimation at $x/D = 31.00$, 40.00 and 51.6 (see figure 2). However, for $x/D = 40.00$ and 51.6 at separation $n = 4$, the decorrelation of noise is small enough so that it is not affecting the estimation for ϵ_{iso1} and ϵ_{iso2}. This is because the streamwise displacement of $4\,\bar{U}\,\Delta t$ is larger than the laser sheet thickness, such that there are completely new particles in the IW used for calculating squares of fluctuating velocity derivatives at two different times. Similarly, for $x/D = 31.00$ at separation $n = 3$, the noise decorrelation is small enough to have a better estimate of ϵ_{iso2} than with $n = 1$.

Appendix B. Integral length scales

In § 4.1, autocorrelation functions of the fluctuating velocities u', v' and w' are presented and discussed, and the integral length scales $\mathcal{L}_{u_i}$ (where $u_i = [u'; v'; w']$ with increasing i from $i = 1$ to $i = 3$) are calculated on the basis of (4.1) by integrating the autocorrelation function up to the first zero crossing τ_c. This approach follows the methodology of Zheng *et al.* (2023*a*) and (2023*b*), which we adopt in the present paper. However, integral scales are often defined based on an integration over a wider time range. Even though such length scales are not useful for the methodology we follow here, in this appendix we calculate integral length scales $\mathcal{L}^{\tau}_{u_i}$ defined similarly to (4.1) but with τ_c replaced by an arbitrary τ.

The ratios $\mathcal{L}^{\tau}_{u}/\mathcal{L}_v$, $\mathcal{L}^{\tau}_{v}/\mathcal{L}_v$ and $\mathcal{L}^{\tau}_{w}/\mathcal{L}_w$ are reported in the left, middle and right columns, respectively, of figure 17. The autocorrelation function ρ'_u asymptotes to a finite value for $x/D = 31.00$, 40.00 and 51.6 as indicated in figure 6 and this causes the ratio $\mathcal{L}^{\tau}_{u}/\mathcal{L}_v$ to increase with increasing x_τ/D as the integration cutoff τ increases. However, as τ increases, the ratios $\mathcal{L}^{\tau}_{v}/\mathcal{L}_v$ and $\mathcal{L}^{\tau}_{w}/\mathcal{L}_w$ asymptote approximately around a finite value: as $x_\tau/D \to 3$, the ratios $\mathcal{L}^{\tau}_{v}/\mathcal{L}_v$ and $\mathcal{L}^{\tau}_{v}/\mathcal{L}_v$ fluctuate around 0.55 ± 0.18. Note that as τ increases the number of data points contributing to the correlation decreases and the statistical error on ρ_{u_i} increases. Even so, we checked that the exponents n and the R^2 coefficients in figures 11–14 are similar if not identical if the length scales $\mathcal{L}^{\tau}_{v}$ and $\mathcal{L}^{\tau}_{w}$ at $x_\tau/D = 3$ are used instead of $\mathcal{L}_v$ and $\mathcal{L}_w$.

References

Alves Portela, F., Papadakis, G. & Vassilicos, J.C. 2018 Turbulence dissipation and the role of coherent structures in the near wake of a square prism. *Phys. Rev. Fluids* **3** (12), 124609.

Alves-Portela, F. & Vassilicos, J.C. 2022 Inhomogeneous turbulence scalings in a free shear flow. In *Proceedings of the 12th International Symposium on Turbulence and Shear Flow Phenomena (TSFP12)*, pp. 1–6. TSFP Organisation.

Apostolidis, A., Laval, J.P. & Vassilicos, J.C. 2022 Scalings of turbulence dissipation in space and time for turbulent channel flow. *J. Fluid Mech.* **946**, A41.

Ashok, A., Van Buren, T. & Smits, A.J. 2015 Asymmetries in the wake of a submarine model in pitch. *J. Fluid Mech.* **774**, 416–442.

Batchelor, G.K. 1953 *The Theory of Homogeneous Turbulence*. Cambridge University Press.

Beaumard, P., Bragança, P., Cuvier, C., Steiros, K. & Vassilicos, J.C. 2024 Scale-by-scale non-equilibrium with Kolmogorov-like scalings in non-homogeneous stationary turbulence. *J. Fluid Mech.* **984**, A35.

Cafiero, G., Obligado, M. & Vassilicos, J.C. 2020 Length scales in turbulent free shear flows. *J. Turbul.* **21** (4), 243–257.

Cafiero, G. & Vassilicos, J.C. 2019 Non-equilibrium turbulence scalings and self-similarity in turbulent planar jets. *Proc. R. Soc. A* **475** (2225), 20190038.

Carlier, J. & Stanislas, M. 2005 Experimental study of eddy structures in a turbulent boundary layer using particle image velocimetry. *J. Fluid Mech.* **535**, 143–188.

Castro, I.P. 2016 Dissipative distinctions. *J. Fluid Mech.* **788**, 1–4.

Chen, J.G., Cuvier, C., Foucaut, J.-M., Ostovan, Y. & Vassilicos, J.C. 2021 A turbulence dissipation inhomogeneity scaling in the wake of two side-by-side square prisms. *J. Fluid Mech.* **924**, A4.

https://doi.org/10.1017/jfm.2026.11161 Published online by Cambridge University Press

CHEN, J.G. & VASSILICOS, J.C. 2022 Scalings of scale-by-scale turbulence energy in non-homogeneous turbulence. *J. Fluid Mech.* **938**, A7.

CIMARELLI, A., MOLLICONE, J.-P., VAN REEUWIJK, M. & DE ANGELIS, E. 2021 Spatially evolving cascades in temporal planar jets. *J. Fluid Mech.* **910**, A19.

COUDERT, J.M. & SCHON, J.P. 2001 Back-projection algorithm with misalignment corrections for 2D3C stereoscopic PIV. *Meas. Sci. Technol.* **12** (9), 1371.

FRISCH, U. 1995 *Turbulence: the Legacy of AN Kolmogorov*. Cambridge University Press.

GEORGE, W.K. & STANISLAS, M. 2021 On the noise in statistics of PIV measurements. *Exp. Fluids* **62** (9), 188.

GLEDZER, E. 1997 On the Taylor hypothesis corrections for measured energy spectra of turbulence. *Phys. D: Nonlinear Phenomena* **104** (2), 163–183.

GOTO, S. & VASSILICOS, J.C. 2015 Energy dissipation and flux laws for unsteady turbulence. *Phys. Lett. A* **379** (16-17), 1144–1148.

GOTO, S. & VASSILICOS, J.C. 2016a Local equilibrium hypothesis and Taylor's dissipation law. *Fluid Dyn. Res.* **48** (2), 021402.

GOTO, S. & VASSILICOS, J.C. 2016b Unsteady turbulence cascades. *Phys. Rev. E* **94** (5), 053108.

KEWALRAMANI, G., JI, B., DOSSMANN, Y., BECKER, S., GRADECK, M. & RIMBERT, N. 2024 A simple analytical model for turbulent kinetic energy dissipation for self-similar round turbulent jets. *J. Fluid Mech.* **983**, A44.

LAIZET, S., NEDIĆ, J. & VASSILICOS, J.C. 2015 Influence of the spatial resolution on fine-scale features in DNS of turbulence generated by a single square grid. *Int. J. Comput. Fluid D.* **29** (3-5), 286–302.

LAVOIE, P., AVALLONE, G., DE GREGORIO, F., ROMANO, G.P. & ANTONIA, R.A. 2007 Spatial resolution of PIV for the measurement of turbulence. *Exp. Fluids* **43**, 39–51.

LECORDIER, B. & TRINITE, ML 2004 Advanced PIV algorithms with image distortion validation and comparison using synthetic images of turbulent flow. In *Particle Image Velocimetry: Recent Improvements: Proceedings of the EUROPIV. 2 Workshop held in Zaragoza, Spain, March 31–April 1, 2003*, pp. 115–132. Springer.

MORA, D.O., MUÑIZ PLADELLORENS, E., RIERA TURRÓ, P., LAGAUZERE, M. & OBLIGADO, M. 2019 Energy cascades in active-grid-generated turbulent flows. *Phys. Rev. Fluids* **4** (10), 104601.

NEKKANTI, A., NIDHAN, S., SCHMIDT, O.T. & SARKAR, S. 2023 Large-scale streaks in a turbulent bluff body wake. *J. Fluid Mech.* **974**, A47.

OBLIGADO, M., DAIRAY, T. & VASSILICOS, J.C. 2016 Nonequilibrium scalings of turbulent wakes. *Phys. Rev. Fluids* **1** (4), 044409.

OBLIGADO, M. & VASSILICOS, J.C. 2019 The non-equilibrium part of the inertial range in decaying homogeneous turbulence. *Europhys. Lett.* **127** (6), 64004.

ORTIZ-TARIN, J.L., NIDHAN, S. & SARKAR, S. 2021 High-Reynolds-number wake of a slender body. *J. Fluid Mech.* **918**, A30.

POPE, S.B. 2000 *Turbulent Flows*. Cambridge University Press.

SCARANO, F. 2001 Iterative image deformation methods in PIV. *Meas. Sci. Technol.* **13** (1), R1.

SOLOFF, S.M., ADRIAN, R.J. & LIU, Z.C. 1997 Distortion compensation for generalized stereoscopic particle image velocimetry. *Meas. Sci. Technol.* **8** (12), 1441.

SREENIVASAN, K.R. 1984 On the scaling of the turbulence energy dissipation rate. *Phys. Fluids* **27** (5), 1048–1051.

STEIROS, K. 2021 Self-regulating turbulence. arXiv preprint arXiv:2101.00609.

TENNEKES, H. & LUMLEY, J.L. 1972 *A First Course in Turbulence*. MIT press.

TOKGOZ, S., ELSINGA, G.E., DELFOS, R. & WESTERWEEL, J. 2012 Spatial resolution and dissipation rate estimation in Taylor–Couette flow for tomographic PIV. *Exp. Fluids* **53**, 561–583.

TOWNSEND, A.A. 1949 Momentum and energy diffusion in the turbulent wake of a cylinder. *Proc. R. Soc. Lond. Series A. Math. Phys. Sci.* **197** (1048), 124–140.

TOWNSEND, A.A. 1976 *The Structure of Turbulent Shear Flow*. Cambridge University Press.

UBEROI, M.S. & FREYMUTH, P. 1970 Turbulent energy balance and spectra of the axisymmetric wake. *Phys. Fluids* **13** (9), 2205–2210.

VALENTE, P.C. & VASSILICOS, J.C. 2014 The non-equilibrium region of grid-generated decaying turbulence. *J. Fluid Mech.* **744**, 5–37.

VASSILICOS, J.C. 2015 Dissipation in turbulent flows. *Annu. Rev. Fluid Mech.* **47** (1), 95–114.

VASSILICOS, J.C. & LAVAL, J.P. 2024 Scale-by-scale non-equilibrium in turbulent flows. In *Coarse Graining Turbulence: Modeling and Data-Driven Approaches and their Applications* (ed. Fernando F. Grinstein, Filipe S. Pereira and Massimo Germano). Cambridge University Press.

WACLAWCZYK, M., NOWAK, J.L. & MALINOWSKI, S.P. 2022*a* Non-equilibrium dissipation scaling in atmospheric turbulence, *J. Phys.: Conf. Ser.* **2367**, 012032.

https://doi.org/10.1017/jfm.2026.11161 Published online by Cambridge University Press

WACLAWCZYK, M., NOWAK, J.L., SIEBERT, H. & MALINOWSKI, S.P. 2022*b* Detecting nonequilibrium states in atmospheric turbulence. *J. Atmos. Sci.* **79** (10), 2757–2772.

WIENEKE, B. 2005 Stereo-PIV using self-calibration on particle images. *Exp. Fluids* **39**, 267–280.

WILLIAMS, O.J.H. & SMITS, A.J. 2024 Asymmetries in nominally symmetric flows. *Annu. Rev. Fluid Mech.* **57**, 35–60.

ZARIPOV, D., LI, R. & DUSHIN, N. 2019 Dissipation rate estimation in the turbulent boundary layer using high-speed planar particle image velocimetry. *Exp. Fluids* **60**, 1–16.

ZHENG, Y., KOTO, N., NAGATA, K. & WATANABE, T. 2023*a* Unsteady dissipation scaling of grid turbulence in the near-field region. *Phys. Fluids* **35** (9), 95–131.

ZHENG, Y., NAGATA, K. & WATANABE, T. 2021 Turbulent characteristics and energy transfer in the far field of active-grid turbulence. *Phys. Fluids* **33** (11), 115–119.

ZHENG, Y., NAKAMURA, K., NAGATA, K. & WATANABE, T. 2023*b* Unsteady dissipation scaling in static-and active-grid turbulence. *J. Fluid Mech.* **956**, A20.

https://doi.org/10.1017/jfm.2026.11161 Published online by Cambridge University Press